Editors' Suggestion

SuperKEKB vacuum system operation in the last 6 years operation

Y. Suetsugu[1,*] K. Shibata,[1,2] T. Ishibashi[1,2] M. Shirai,[1] S. Terui[1]
K. Kanazawa,[1] H. Hisamatsu,[1] and M. L. Yao[2]

[1]*KEK, Oho, Tsukuba, Ibaraki 305-0801, Japan*
[2]*SOKENDAI, Shonan Village, Hayama, Kanagawa 240-0193, Japan*

The operation of the SuperKEKB has been ongoing since 2016. The vacuum systems of the main ring (MR) which consists of a 7-GeV electron ring (HER) and a 4-GeV positron ring (LER), the damping ring (DR) for 1.1 GeV positrons in the middle of the injector linac have been working well as a whole. As of June 2022, the maximum stored beam currents of MR are 1.46 and 1.14 A for the LER and the HER, respectively, and approximately 30 mA for the DR. The pressure increase per unit beam current is steadily decreasing and the new vacuum components developed for the SuperKEKB have been working as expected. No significant electron cloud effect has been observed in the LER after installing solenoids in drift spaces in 2017 which apply magnetic fields in the beam direction. The recent pressure behavior of the LER with increased beam current is explained by considering thermal gas desorption induced by the beam as well as photon-stimulated gas desorption. Currently, the beam lifetime is primarily limited by the Touschek effect rather than the vacuum pressure, and their degrees of contribution are evaluated. The challenges associated with high beam currents, such as damage to beam-collimator heads and excess heating of beam pipes at wiggler sections have become more apparent as beam currents are increased. The status of the SuperKEKB vacuum system and the experiences during the past 6 years of operation are presented here.

I. INTRODUCTION

The SuperKEKB is an electron-positron collider with asymmetric energies operating at KEK in search of a new physics in the B-meson regime with an unprecedented high luminosity utilizing a "nanobeam collision scheme" (Fig. 1) [1–3]. The main ring (MR) consists of a high-energy ring (HER) for 7 GeV electrons and a low energy ring (LER) for 4 GeV positrons each having a circumference of approximately 3 km (Fig. 2). Beam operations for the facility started in 2016. Following the installation and commissioning of the damping ring (DR) for 1.1 GeV positrons at the injector linac, the full-scale physics experiment using the complete Belle II detector has been in operation since 2019. Moreover, the SuperKEKB has been breaking the world record for luminosity every year since 2020 [3]. During this time, the vacuum systems of the LER, HER, and DR have been working well [4–7]. Figure 3

shows the layout of the LER and HER beam pipes as well as the bellows chambers in the MR tunnel. As of June 2022, the maximum stored beam currents for the LER and HER are 1.46 and 1.14 A, and approximately 30 mA for the DR.

The various vacuum components which have been developed for SuperKEKB [8–10] have been operating as expected. Pressure increases per unit of beam current

FIG. 1. SuperKEKB at KEK Tsukuba campus.
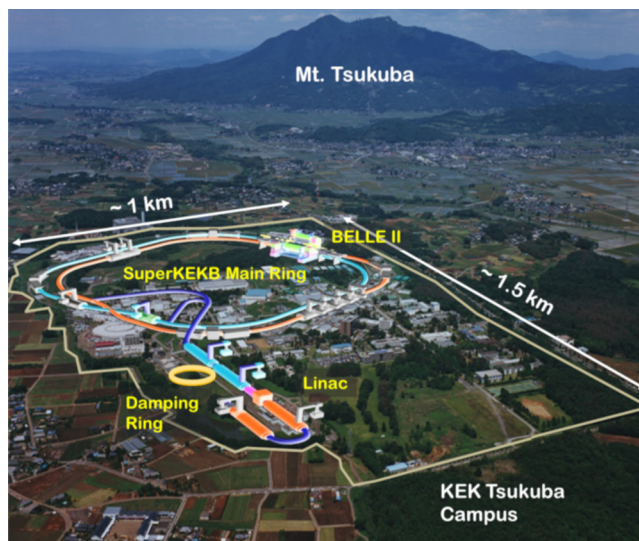
*Corresponding author.
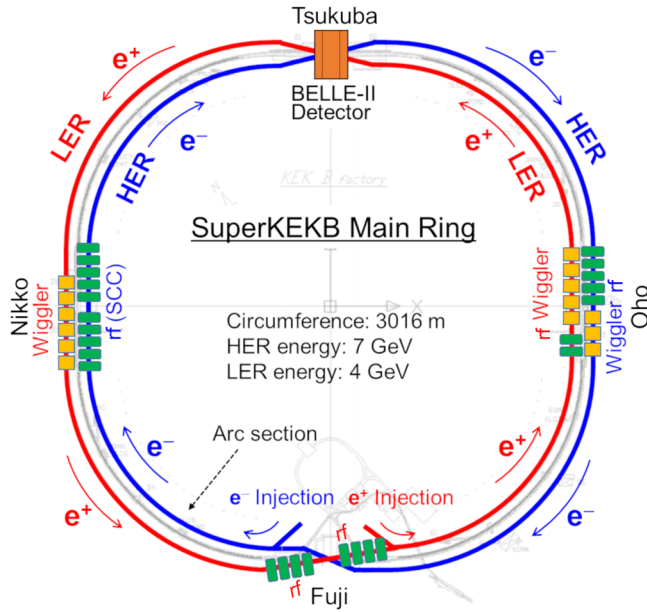yusuke.suetsugu@kek.jp, KEK, 1-1 Oho, Tsukuba, Ibaraki, 305-0801, Japan.

FIG. 2. Layout of the SuperKEKB Main Ring (MR). One ring consists of four arc sections, four straight sections, and one collision point at Tsukuba (Belle II).
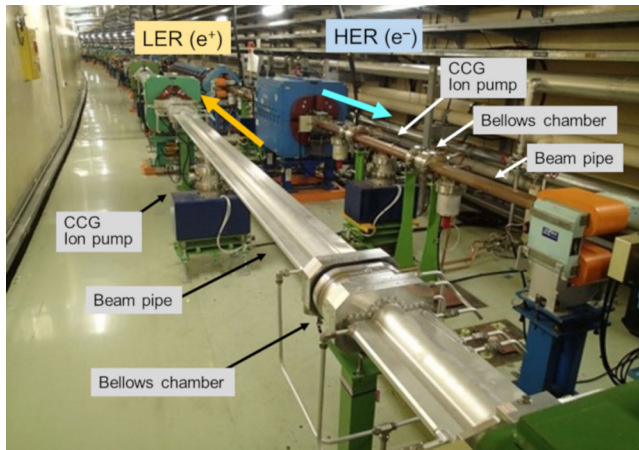

FIG. 3. Layout of the beam pipes, bellows chambers, ion pumps, and CCGs for LER and HER in the MR tunnel.

$(\Delta P/\Delta I)$ in the arc sections have been steadily decreasing with integrated beam currents (beam dose) in each ring [11]. These pressure increases are mainly the photon desorption caused by synchrotron radiation (SR). In addition to this, the pressure increases by thermal desorption from the beam induced heating due to higher beam currents, especially in LER. Currently, beam lifetimes are primarily determined by the Touschek effect rather than by scattering due to residual gases in the vacuum chamber. Strong electron cloud effects (ECE) in the LER have not been observed in normal operations after magnetic fields in the beam direction were applied in drift spaces [12,13]. In this article, we provide a global presentation of

the SuperKEKB vacuum system and the experiences from the past 6 years of operation.

II. OPERATION HISTORY

To achieve the unprecedented high luminosity in the SuperKEKB, the existing KEKB vacuum system has undergone a series of upgrades [2] during a 6-year period starting in 2010. Newly fabricated beam pipes and vacuum components have been installed in approximately 93% of the LER and 20% of the HER [8–10].

The first commissioning phase (Phase 1), was dedicated to tuning the accelerator and was conducted between February and June of 2016 [14]. Beam currents of up to 1 A were used to study the vacuum scrubbing of beam pipes, the electron cloud effect (ECE) in the LER, and the stability of the new vacuum components [4,5,11]. The Belle II particle detector [15] and its related vacuum components, new beam pipes for the LER injection region, and beam collimators [16] were installed during the subsequent long shutdown period between July 2016 and June 2018. During this time, various countermeasures were also implemented to overcome the challenging problems encountered during the Phase-1 commissioning period [14,17]. The main objective of the second commissioning phase (Phase 2) was beam collision tuning, which took place between March and July of 2018 [18,19]. Starting in March 2019, Phase-3 commissioning began with a full-scale physics run including the complete Belle II detector and newly installed DR in the middle of the linac [20]. To date, Phase-3 commissioning is still running with continuous performance improvement efforts [3].

Trends of the average vacuum pressures and beam currents for the LER and HER, from the start of Phase 3 till June 2022, are presented in Figs. 4(a) and 4(b), respectively. Here, the suffix "ab" refers to the spring operation (usually from February to June) until the summer shutdown and the suffix "c" refers to autumn operation (usually from October to December). Pressures measurements show a steady decrease during this period while gradually increasing beam currents. The observed pressure spikes correspond to periods of operations just after long shutdowns where interventions, including the exposure of vacuum components to air, were required or to periods where the NEG (non-evaporable getter) pumps (main pumps in SuperKEKB) [21] were activated. It should be noted that the pressure values shown in Fig. 4 correspond to 3 times the actual reading (nitrogen equivalent) of the CCG (cold cathode gauge) which is located just above a sputtering ion pump. This factor of "3" was estimated from a simulation taking into the conductance of rf-shield screen between the beam channel and the pumping port and that of the pumping port itself. These gauges are located approximately every 10 m along the ring (Fig. 3) to measure the pressure in the beam pipe. The measurement limit of the CCG controllers (1×10^{-8} Pa) imposes a
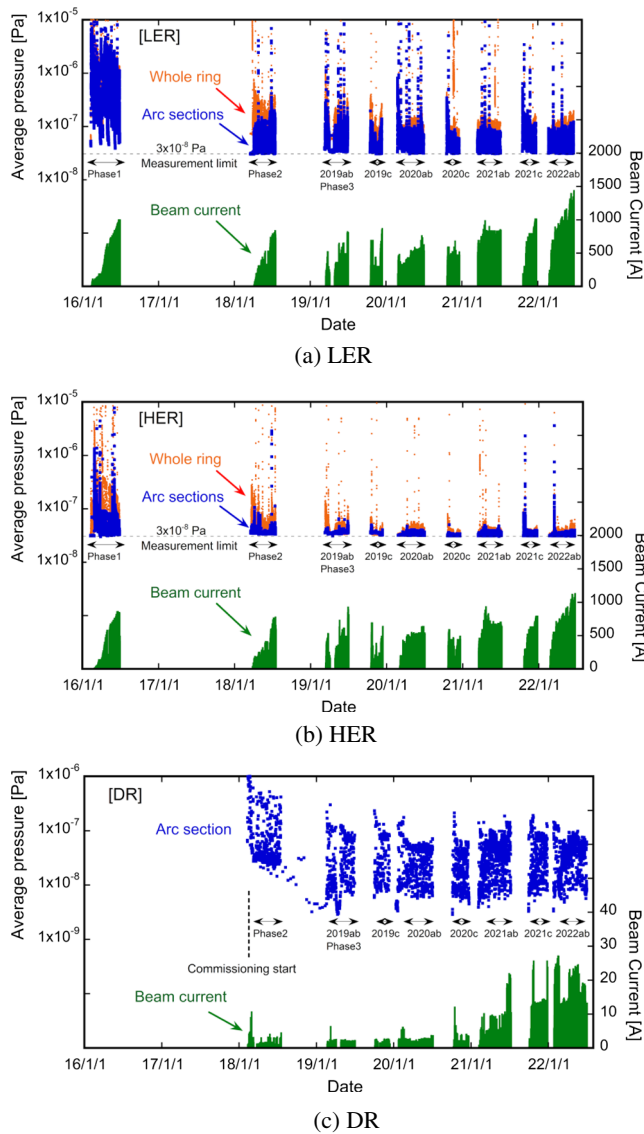
FIG. 4. Trends of pressures and beam currents since Phase-1 commissioning in 2016 for (a) LER, (b) HER, and (c) DR.

FIG. 5. Total operation time and the number of faults by year. The number of faults related to the vacuum system is indicated in red.

minimum pressure measurement limit of 3×10^{-8} Pa. Given this limit, measured pressures in this range are not very reliable. In June 2022, the average pressure with beams was 2.0×10^{-7} Pa (1.46 A, 2249 bunches) for the LER and 4.9×10^{-8} Pa (1.14 A, 2249 bunches) for the HER. The longitudinal rms bunch length was approximately 10 mm and each bunch contains approximately 1011 charged particles. Without stored beams, the base pressures in both the LER and HER are near the measurement limit of approximately 3×10^{-8} Pa.

The DR vacuum system has been working well since the start of its operation in 2019 [6,22]. The trends of the average vacuum pressure and beam currents from the start of operation in 2019 till July 2022 are presented in Fig. 4(c). The maximum stored beam current is approximately 30 mA. As of July 2022, the total beam dose has reached
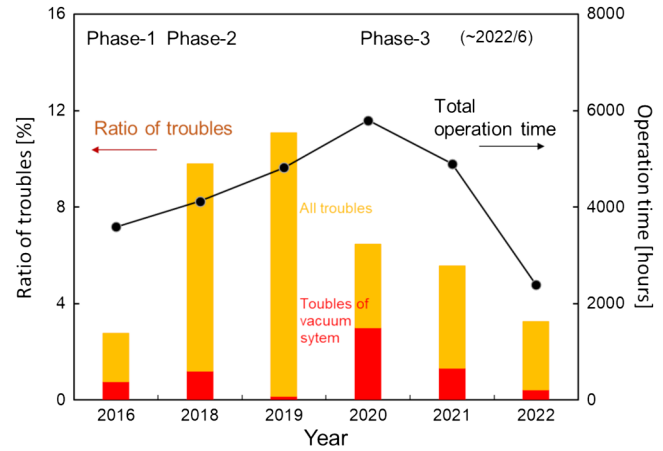
approximately 67.6 A h. The base pressure and the pressure with the maximum beam current stored are approximately 1×10^{-8} and 1×10^{-7} Pa, respectively. The DR vacuum pressure is estimated using the discharge current of sputtering ion pumps [6]. The base pressure is close to the measurement limit as in the case of MR.

Figure 5 shows the total operation time during the three commissioning phases as well as the number of faults for each year. The total number of faults includes those related to the vacuum system, which is shown in red. Vacuum faults include repairs of air leaks and exchanges of damaged vacuum components. Faults related to the vacuum system were less than 4% each year during all 6 years of operations.

For the SuperKEKB upgrade, various new vacuum components were installed to mitigate the expected challenges due to high beam currents such as beam instabilities due to beam impedances and electron cloud effects in the positron ring (LER). Examples of newly installed components are bellows chambers and gate valves with a comb-type rf-shield [23], step-less Matsumoto-Ohtsuka type flanges to reduce beam impedances [24] and beam pipes with antechambers [25]. To counter ECE [12,13], TiN (Titanium Nitride) film coatings [26], clearing electrodes [27], and groove structures [28] were also installed. A new style of beam collimator was also installed to suppress the Belle-II detector background [16,29]. Most of these components have been working as expected. The temperatures during beam operations for bellow chambers and gate valves with comb-type rf shields are shown in Figs. 6(a) and 6(b), respectively. The temperatures of these components at the wiggler sections are higher than in other sections and are attributed to Synchrotron Radiation (SR). The SR power is highest at the wiggler section leading to the higher temperature of components. The status of ECE and beam collimators will be discussed later.
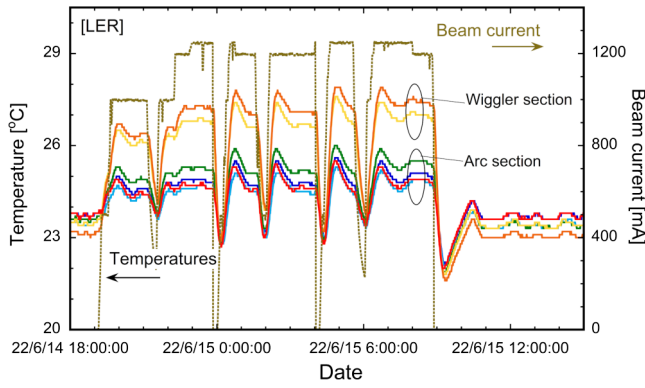
(a) Bellows chambers
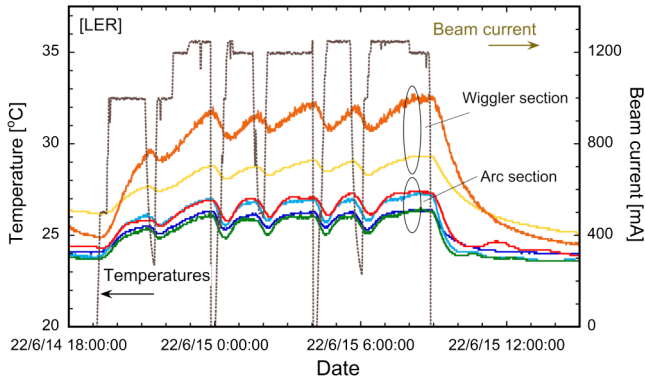
(b) Gate valves

FIG. 6. Typical temperatures of (a) bellows chambers and (b) gate valves at wiggler and arc sections during a recent operation.

III. PRESSURE RISE DURING OPERATION

### A. Pressure rises per unit beam current (vacuum scrubbing)

The pressure increase per unit beam current ($\Delta P/\Delta I$) compared to the beam dose [integrated beam currents (A h)] in the arc sections of the LER and HER is shown in Figs. 7(a) and 7(b), respectively. These values are also plotted using the photon-stimulated gas desorption rates (η [molecules photon^{-1}]) and the photon doses (integrated numbers of photons per unit length [photons m^{-1}]) on the same plots. $\Delta P/\Delta I$ and η are representative figures of merit for evaluating the performance of the accelerator vacuum system. The pressures indicated in these figures are the average values for the arc sections in the ring and correspond to 3 times the reading values of the CCGs, as explained above. In these areas, the pumping speed per unit length is 0.06 and 0.03 m^3 s^{-1} m^{-1} is assumed for the LER and HER, respectively [5]. In the calculation of ΔP, a base pressure of 3×10^{-8} Pa is used, and only pressure values at beam currents higher than 40% of the maximum stored current were considered to avoid uncertainty near the base pressure. Spikes in $\Delta P/\Delta I$ correspond to times just after long shutdowns, as described above. $\Delta P/\Delta I$ for the
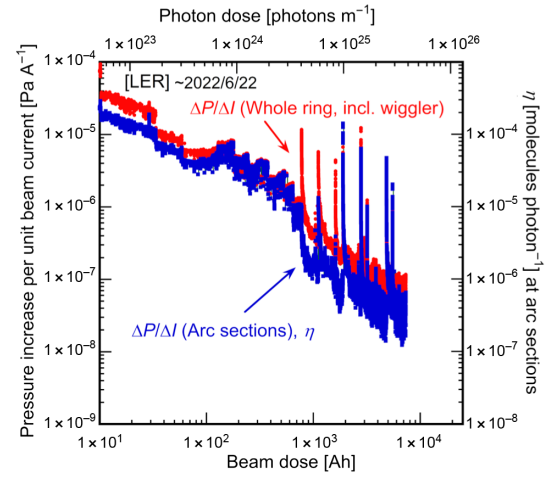
(a) LER
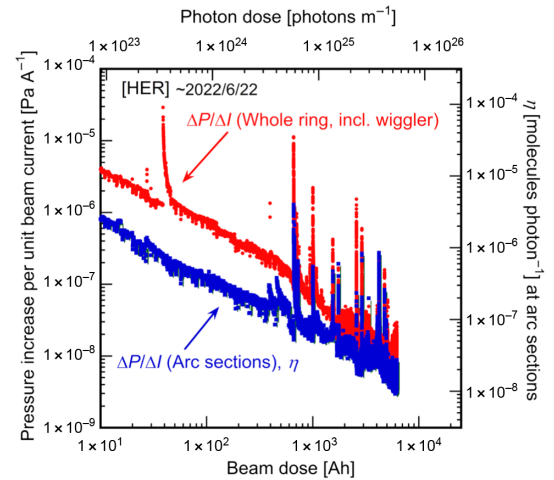
(b) HER
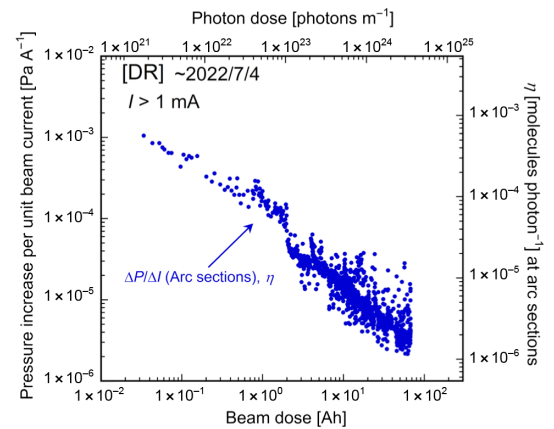
(c) DR

FIG. 7. Pressure increase per unit beam current ($\Delta P/\Delta I$) of the whole rings and arc sections as a function of the beam dose, and η of arc sections as a function of photon dose for (a) LER, (b) HER, and (c) DR from 2016.

arc sections in the LER ring is 6.5×10^{-8} Pa A^{-1} and η is 3×10^{-7} molecules photon^{-1} as of June 2022. This is after a beam dose of 7310 A h which corresponds to a photon dose of 3.87×10^{25} photons m^{-1}. For comparison, $\Delta P/\Delta I$

in the HER ring is 1.1×10^{-8} Pa A^{-1} and η is 2×10^{-8} molecules photon^{-1} after a beam dose is 6200 A h which is a photon dose of 5.74×10^{25} photons m^{-1}. The values of $\Delta P/\Delta I$ and η for the HER are lower than those of the LER because most of the beam pipes and components in the HER arc sections were reused from the existing KEKB accelerator. The surfaces of these components were already conditioned by SR and exhibit the so-called "Memory effect" [30,31].

Figure 7(c) shows the values of $\Delta P/\Delta I$ and η for the DR. These values are steadily decreasing with beam conditioning time and the resulting photon doses. As of July 2022, $\Delta P/\Delta I$ was 3.5×10^{-6} Pa A^{-1} and η is 1.8×10^{-6} molecules photon^{-1} with a beam dose of 67.6 A h and a photon dose of 3.47×10^{24} photons m^{-1}. In the DR, values of pressure with beam currents higher than 1 mA were considered for the calculation, and the pumping speed was assumed to be 0.04–0.05 m^3 s^{-1} at the inlets of the pumping ports [6]. The values of pressure were estimated from the discharge currents of sputtering ion pumps.

B. Beam current dependence on pressures

As shown in Figs. 7(a) and 7(b), the recent values of $\Delta P/\Delta I$ for the MR at high beam doses are scattered compared to those at lower beam doses. This implies that the pressure rise is not simply proportional to the beam current or, put another way, that the pressure rise is not solely a result of the photon desorption due to SR.

Figure 8(a) shows the dependence of the pressure on the total beam current for the LER between the 16th of March to the 25th of April 2022. Here pressure values above 6×10^{-8} Pa (twice the base pressure) are plotted using different colors. (These values were used in a multiple regression analysis (MRA) described later.) The different colors correspond to a different number of bunches (N_b) in the beam. The change in N_b is accomplished by adjusting the interval of bunches, that is, the bunch spacing. The pressure values shown were taken when the stored beam current was greater than 100 mA and stable for over 1 min. It can be seen in this figure that the pressure increase is not linear with the current, and the rate of pressure increase becomes higher with increasing current. Furthermore, the pressure behavior depends on N_b and not just the current being stored.

We aim to explain the behaviors of pressure versus current in the LER by including the effects of thermal gas desorption due to the heating of the beam pipes and other vacuum components as well as the photon desorption due to the SR. Here we assume a constant pumping speed, ignoring the beam scrubbing effects, electron-stimulated
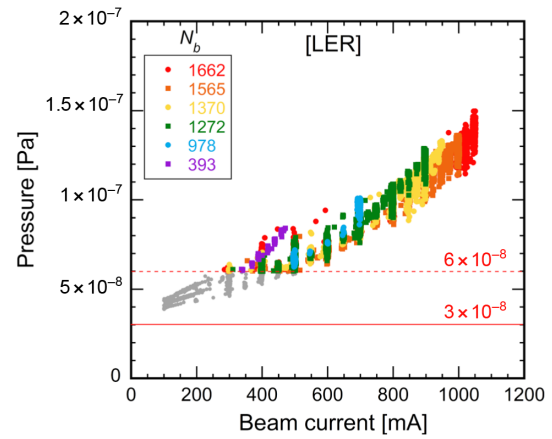
(a) Measurement.
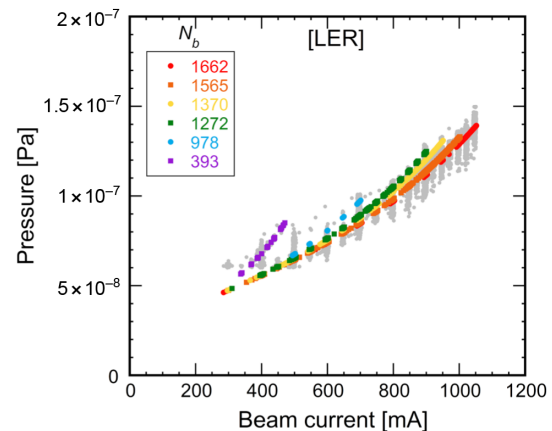
(b) Calculation assuming $\Delta P_t \propto (\Delta T)^2$
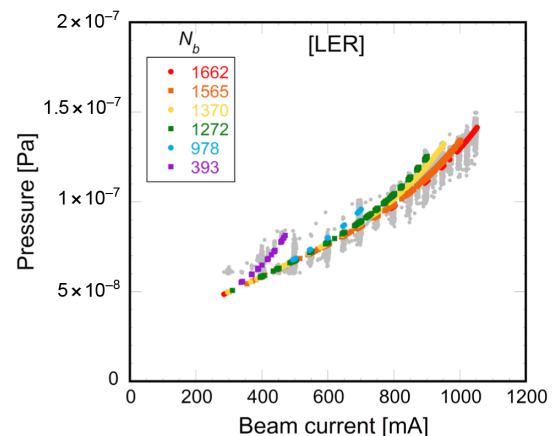
(c) Calculation assuming $\Delta P_t \propto (\Delta T)^3$

FIG. 8. Dependences of P on I (a) measured, (b) calculated using the regression curve derived assuming $\Delta P_t \propto (\Delta T)^2$, and (c) those derived assuming $\Delta P_t \propto (\Delta T)^3$ for several N_b of 393–1662 for LER, where the P values higher than 6×10^{-8} Pa from the 16th of March to 25th of April 2022 were used for the MRA. Gray points represent all data.

gas desorption, and beam-size blowup due to the ECE during the period in question [5].

For the photon desorption, the pressure rise (ΔP_p) should be proportional to the number of photons irradiated onto the surface. Therefore, at constant beam energy, ΔP_p is proportional to the current,

$$\Delta P_p \propto I. \qquad (1)$$

For thermal desorption, we assume that an equilibrium is almost established between molecules in the vacuum space and molecules on the surface [32]. Under this assumption, the following equation holds:

$$c_s \frac{P_t}{\sqrt{2\pi m k_B T}} = \frac{\sigma}{\tau} = \frac{\sigma}{\tau_0} \exp\left(-\frac{E_d}{RT}\right), \qquad (2)$$

where c_s is the adsorption probability, P_t is the pressure (Pa), m is the molecular mass (kg), k_B is Boltzmann constant (1.381×10^{-23} J K^{-1}), T is the temperature (K), σ is the adsorbed amount on the surface, τ is the mean residence time for adsorption, τ_0 is a constant around 10^{-13} sec, E_d is the adsorption energy of gas molecules (J mol^{-1}), and R is the gas constant (8.314 J mol^{-1} K^{-1}). The order of the desorption process is assumed to be 1. Considering that the temperature range in question is narrow and near room temperature, that is, 293–323 K (20–50 °C), the dependence of P_t on T can be written as follows:

$$P_t \propto \exp\left(-\frac{E_d}{RT}\right). \qquad (3)$$

Here the dependences of σ, the velocity of molecules ($\propto \sqrt{T}$), and c_s on T are much smaller than the exponential dependence of τ, and thus are neglected in Eq. (3). Therefore, the pressure rise (ΔP_t), when T increased to $T + \Delta T$, is the difference between P_t at $T + \Delta T$ and T in Eq. (3);

$$\Delta P_t \propto \exp\left(-\frac{E_d}{R(T+\Delta T)}\right) - \exp\left(-\frac{E_d}{RT}\right). \qquad (4)$$

However, since the dependence of ΔP_t on ΔT in Eq. (4) is exponential and complicated, the MRA using ΔT due to the beam current as an explanatory variable is difficult. Considering that the range of T in question is relatively narrow around room temperature, we approximate the exponential function of ΔT in Eq. (4) by a power function of ΔT. Because the main desorbed gas at these low temperatures (293–323 K) is water with an adsorption energy (E_d) of 50–100 kJ mol^{-1} [33], from a simple calculation, ΔP_t is found to be well approximated by $(\Delta T)^2$ or $(\Delta T)^3$;
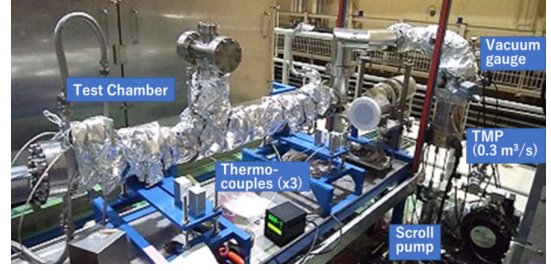
(a) Experimental setup
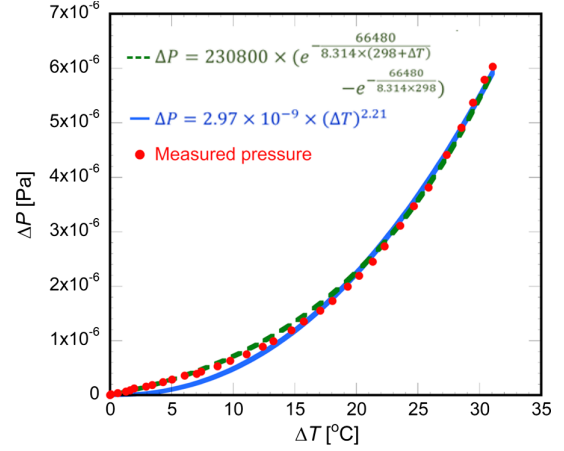
(b) Results

FIG. 9. (a) Experimental setup to measure the dependence of ΔP_t on ΔT, and (b) the measured results and calculated ΔP_t using the regression curves derived assuming Eqs. (4) and (5).

$$\Delta P_t \propto (\Delta T)^{2\sim3}. \qquad (5)$$

To confirm this approximation, the pressure rise due to a temperature increase was experimentally measured using a test chamber made of Al alloy and a low temperature baking process. The experimental setup is shown in Fig. 9(a). The volume and inner surface area of the test chamber [including the manifolds upstream of the turbo molecular pump (TMP)] are approximately 0.0142 m^3 and 1.793 m^2, respectively. The room temperature during the measurements was 24.5 °C and the base pressure was 6.4×10^{-7} Pa. The test chamber was not baked out before this measurement. The temperature of the chamber was raised at a rate of approximately 1 °C per 5 min up to ∼60 °C. The temperatures reported are the average of three K-type thermocouples which were attached to the surface of the test chamber. The results are shown in Fig. 9(b) along with the regression curves derived from Eqs. (4) and (5). The measured dependence of ΔP versus ΔT agreed well with these regression curves. E_d calculated using Eq. (4) was 66 kJ mol^{-1} and within the expected range. Based on these results, we assume that ΔP_t is proportional to $(\Delta T)^2$.

SR produced by the beam is considered as one possible source of heating. However, this does not depend on N_b and water cooling is applied near or behind any of the

irradiated surfaces. Therefore, the thermal desorption due to SR can be neglected. Other possible sources are the Joule losses due to wall currents and those from higher order modes (HOM) excited by the beams. For both cases, the input power is proportional to the product of the number of bunches (N_b) and the square of current per bunch (I/N_b) [34]. From these considerations, ΔP_t can be expressed as follows:

$$\Delta P_t \propto (\Delta T)^2 \propto \left(\frac{I^2}{N_b}\right)^2. \tag{6}$$

Finally, ΔP and P can be written as follows:

$$\Delta P = \Delta P_p + \Delta P_t = C_p I + C_t \left(\frac{I^2}{N_b}\right)^2. \tag{7}$$

$$\therefore P = P_0 + C_p I + C_t \left(\frac{I^2}{N_b}\right)^2, \tag{8}$$

here P_0 is the base pressure and C_p and C_t are constants. These constants were determined by MRA from the measured pressures in Fig. 8(a) using I and $(I^2/N_b)^2$ as the explanatory variables. Pressures higher than 6×10^{-8} Pa were used to exclude the effect of the CCG measurement limit of 3×10^{-8} Pa mentioned earlier. The number of data points used in the MRA was 42,254 and the obtained regression curve was

$$P = 2.42 \times 10^{-8} + 7.64 \times 10^{-11} I + 7.8 \times 10^{-14} \left(\frac{I^2}{N_b}\right)^2 \text{ (Pa)}. \tag{9}$$

Here the unit of current (I) is mA. Note that the coefficient of determination (R2) of the regression curve was 0.977. The pressures calculated using the regression curve are plotted in Fig. 8(b), and they agree well with the measured values shown in Fig. 8(a). The observed behavior of pressure versus current is well explained by the photon desorption and thermal gas desorption due to the heating by beams. However, as indicated by Eq. (9), the pressure rise is dominated by photon desorption which is given by the second term on the right-hand side of the equation.

A similar analysis was conducted using the same data but assuming that ΔP_t is proportional to $(\Delta T)^3$ instead of $(\Delta T)^2$ in Eq. (6) since the experimental data indicated $\Delta P_t \propto (\Delta T)^{2.2}$ [Fig. 9(b)]. The result is shown in Fig. 8(c). The coefficient of determination (R2) of the regression curve was 0.977, which is similar to the previous case. A very similar result to that in Fig. 8(b) was obtained up to a current value of ~1200 mA. The difference between the two curves starts to become clear at higher values of current and the actual pressure response will be checked in the future as higher currents are stored.
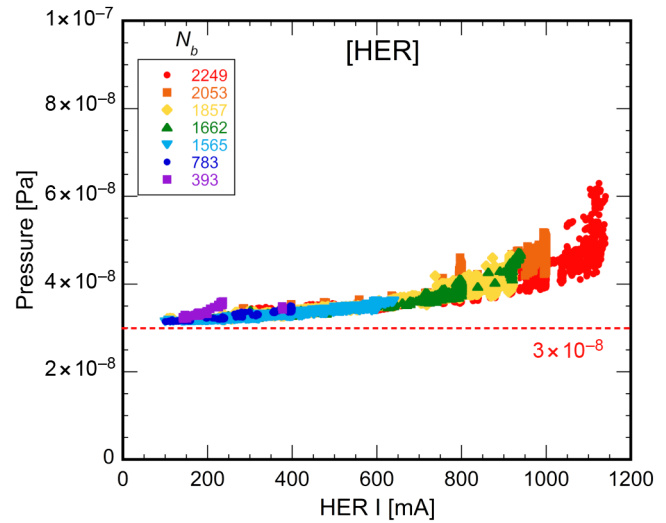

FIG. 10. Dependences of P on I for N_b of 393–2249 for the HER from the 19th of May to the 22nd of June 2022.

As for the HER, the maximum pressure during the operation was approximately 5×10^{-8} Pa as shown in Fig. 10. A similar analysis was applied using all available data points (pressure values higher than 3×10^{-8} Pa) during the period in question. Some dependence on the bunch charge as well as the current was observed similar to the case of the LER. However, since the pressure values are near the measurement limit of the CCGs (3×10^{-8} Pa), the results are not quantitatively reliable. Qualitatively, the thermal desorption seems to affect ΔP in the HER at higher beam currents similar to the LER (see Fig. 10).

IV. BEAM LIFETIME

It is well known that the major factors which limit the beam lifetime (τ) related to the vacuum pressure of an electron or positron storage ring, are bremsstrahlung, Rutherford scattering, and Møller scattering [35]. If the physical aperture of beam pipes is sufficiently large, τ is mainly limited by the bremsstrahlung. In SuperKEKB, the physical aperture at beam collimators is very narrow (~1 mm) in order to suppress the background at the Belle II detector [29,36]. In this case, the effect of the Rutherford scattering can be a major limitation. In the early stage of operation, the vacuum pressure was still high and τ was mostly determined by the interaction between the beam and residual gas molecules, especially for the LER. With beam conditioning, $\Delta P/\Delta I$ has continued to decrease as was shown in Figs. 4 and 7. On the other hand, since the bunch length of the MR is typically 5–6 mm and the beam emittance is small (~20 pm in the vertical direction), τ is now limited by the Touschek effect.

If τ is determined only by pressure, that is, the gas source is mainly due to the photon-desorption, $1/\tau$ can be written as follows:
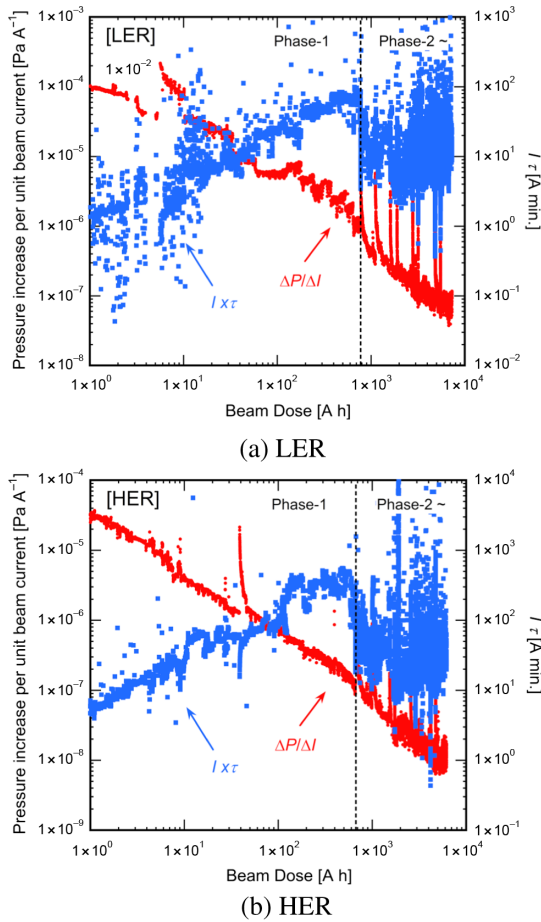
(a) LER

(b) HER

FIG. 11. Behaviors of pressure increase per unit beam current ($\Delta P/\Delta I$) and $I\tau$ as a function of beam dose from 2016 for (a) LER and (b) HER.

(a) LER

(b) HER

FIG. 12. Trends of I, τ, and N_b used for the MRA to estimate the influence of the pressure and Touschek effect on τ from the 15th of May to the 21st of June 2022 for (a) LER and (b) HER (single-beam mode).

$$\frac{1}{\tau} \propto P = \frac{\Delta P}{\Delta I} I \qquad \therefore \frac{\Delta P}{\Delta I} \times I\tau = \text{const.} \qquad (10)$$

Figures 11(a) and 11(b) show $\Delta P/\Delta I$ for the whole ring and $I\tau$ for the LER and HER, respectively, as a function of the beam dose. In both cases, $I\tau$ steadily increased with increasing beam dose during the Phase-1 commissioning along with a corresponding decrease in $\Delta P/\Delta I$. The values of $I\tau$ were approximately 70 A min for the LER and 300 A min for the HER at the end of Phase-1 commissioning. However, $I\tau$ became much smaller after Phase-2 commissioning for both the LER and HER even though $\Delta P/\Delta I$ continued to decrease. This can be explained by two primary factors. First, the Belle II detector was installed and the beam size was squeezed to achieve the small β^* s (beta function values at the collision point) required for collision experiments. Second, the beam collimators were installed, and the physical aperture was decreased in order to protect the final focusing magnets and sensitive detector components. Given these two factors, τ is no longer limited by the vacuum pressure in the storage rings.
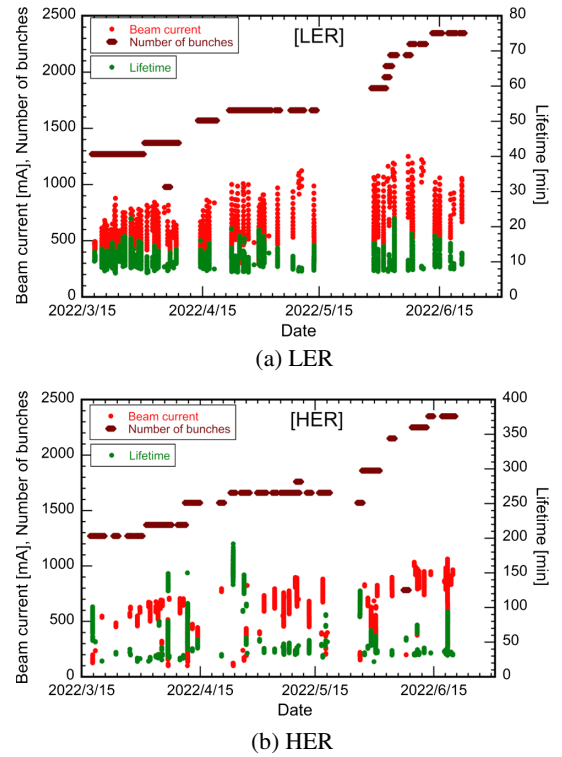
Here, we estimate the beam lifetimes determined by the vacuum pressure and Touschek effect during operation using a similar approach as how ΔP was analyzed in the previous section. We estimate τ only during the single beam mode (i.e., no collision) because there are other mechanisms, such as the change in dynamic aperture and beam emittances due to beam-beam effects during collisions which affect τ in complex ways.

Beam current (I), τ, and N_b are used for the MRA in the LER and are presented in Fig. 12(a). The vertical beta function at the collision point (β_y^*) was 1 mm during this period. The data points used in the MRA are when the values of current were larger than 100 mA and decreasing steadily for at least 1 min and the values of τ were longer than 3 min. Pressure values were higher than 6×10^{-8} Pa, similar to the previous section to avoid the uncertainty of the CCG measurement limit (i.e., 3×10^{-8} Pa). Values of N_b were 978–2346, and the bunch currents were in the range of 0.1–0.7 mA per bunch. The number of data points used in the analysis was 1159.

The dependences of τ on beam current for different N_b and different pressure ranges are shown in Figs. 13(a) and 14(a), respectively. τ depends on N_b as well as beam current and is longer for more bunches with the same current stored (smaller I/N_b) as can be seen in Fig. 13(a).
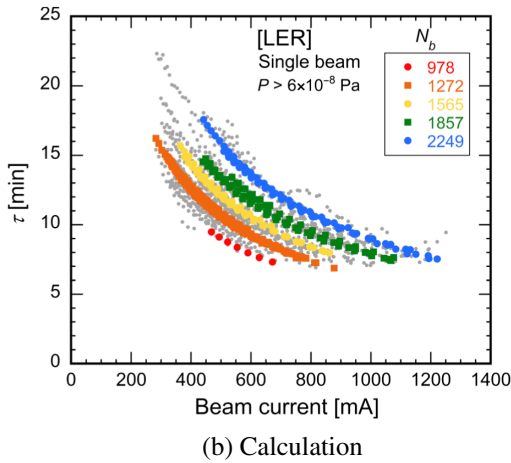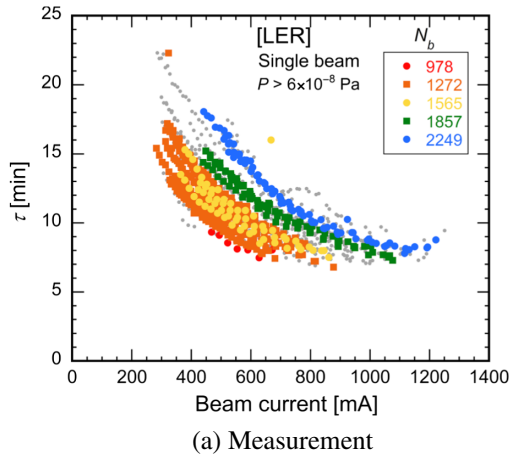
(a) Measurement

(b) Calculation

FIG. 13. Dependence of τ on I (a) measured and (b) calculated using the regression curve for several N_b of 978–2249 for LER, where the P values higher than 6×10^{-8} Pa, from the 15th of May to the 21st of June 2022, were used for the MRA. Gray points correspond to all measured data.

(a) Measurement

(b) Calculation

FIG. 14. Dependence of τ on I (a) measured and (b) calculated using the regression curve for several pressure ranges of 6×10^{-8}–1.6×10^{-7} Pa for the LER, where the data from the 15th of May to the 21st of June 2022, were used for the MRA. Gray points represent all measured data.

In contrast, the dependence of τ on pressure is weak, as indicated in Fig. 14(a).

The beam lifetime (τ_p) determined by the pressure (P) is expressed here as follows:

$$\frac{1}{\tau_p} \propto P. \tag{11}$$

τ_p depends on the gas species as well as their partial pressures remaining in the vacuum system [35,37]. If the main component of τ_p is the Rutherford scattering, then τ_p should be a function of the product of the beta functions and the pressure at the point in question [Eq. (15)]. In order to see the first order effects of τ_p, we simply assumed Eq. (11) here. The value of P is 3 times the average of all CCG readings in the ring, and it is the nitrogen-equivalent value.
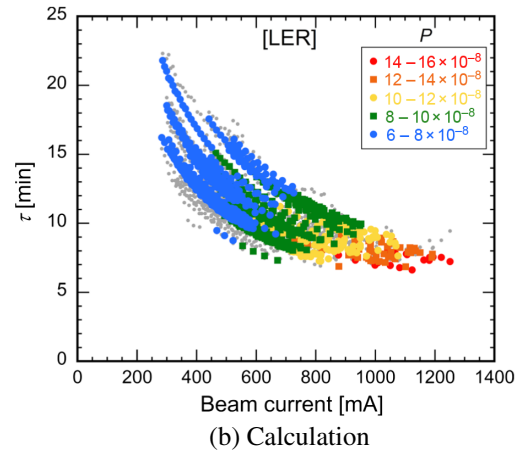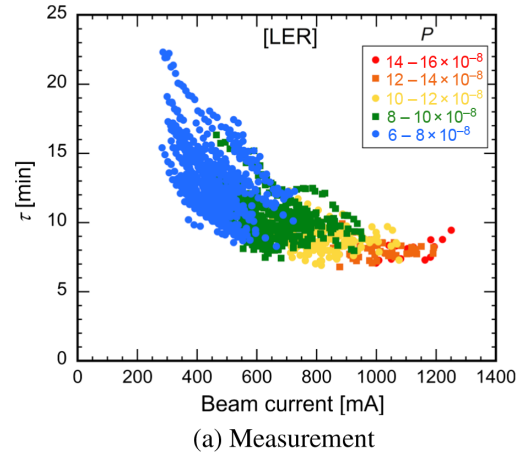
The Touschek lifetime (τ_t) is expressed here as follows:

$$\frac{1}{\tau_t} \propto \frac{I}{N_b \sigma_z}. \tag{12}$$

Here σ_z is the bunch length. Since τ_t is proportional to the beam size in principle [35,38], $1/\tau_t$ should be basically proportional to $I/(N_b \sigma_z \sqrt{\varepsilon_x \varepsilon_y})$ instead of Eq. (12), where ε_x and ε_y are the horizontal and vertical beam emittance, respectively. However, it was found that the measured beam emittances at different operating modes during the period in question (from the 15th of March to the 22nd of June 2022) changed from time to time even with the same beam current, N_b, τ, and P. Beam emittances were measured by x-ray beam size monitors [39], and the bunch length values (σ_z) were calculated as a function of the bunch current (I/N_b) using the approximate formula obtained from a separate experiment [40]. The origin of the changes in emittances has not been fully understood as of yet.
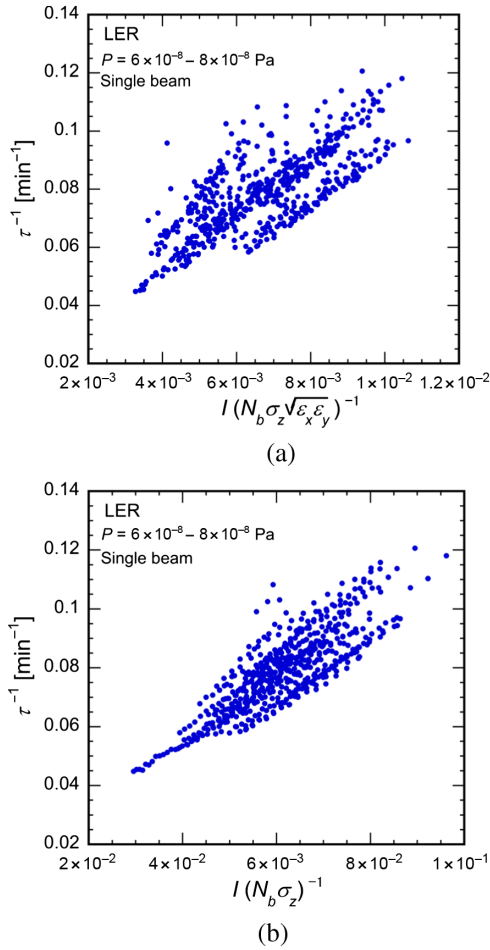
(a)

(b)

FIG. 15. Dependence of $1/\tau$ on (a) $I/(N_b\sigma_z\sqrt{\varepsilon_x\varepsilon_y})$ and (b) $I/(N_b\sigma_z)$ at $P = 6\text{–}8 \times 10^{-8}$ Pa for the LER.

Consequently, the measured $1/\tau_t$ was well expressed by $I/(N_b\sigma_z)$ rather than $I/(N_b\sigma_z\sqrt{\varepsilon_x\varepsilon_y})$ for the same pressure values as is shown in Fig. 15. For this reason, we use Eq. (12) here to express τ_t.

Finally, we assume that τ is determined by the sum of τ_p and τ_t in Eqs. (11) and (12) and can be written as

$$\frac{1}{\tau} = \frac{1}{\tau_p} + \frac{1}{\tau_t} = C_p P + C_t \frac{I}{N_b\sigma_z}, \quad (13)$$

where C_p and C_t are constants. These constants depend on the physical and dynamic apertures of the ring as well as the gas species and their partial pressures around the ring. Here we tried to find these constants using the MRA from the measured pressure, τ, and N_b during the period in question, assuming that the residual gas is only one species, the pressure distribution in the ring is uniform, and there are no changes in the physical and dynamical apertures for the single beam mode during this period.

The MRA was performed under the conditions that $1/\tau$ is zero when $P = 0$ Pa and $I = 0$ mA. The obtained regression curve was
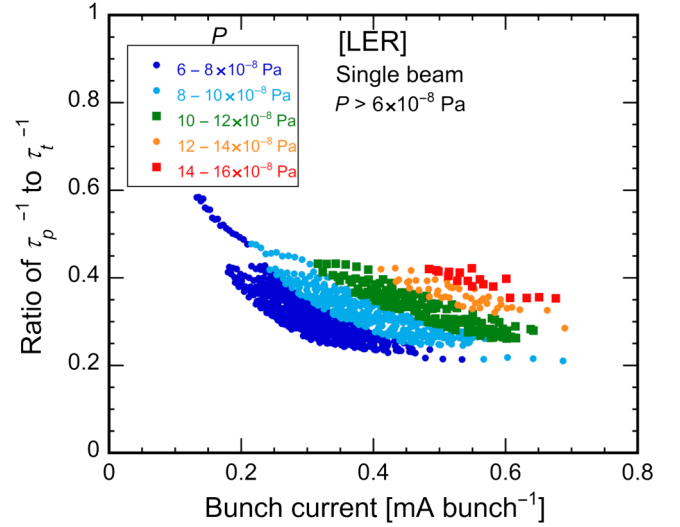

FIG. 16. Ratio of the first term $(1/\tau_p)$ to the second term $(1/\tau_t)$ of the right-hand side of Eq. (14) for the several pressure ranges of $6 \times 10^{-8}\text{–}1.6 \times 10^{-7}$ Pa for the LER.

$$\frac{1}{\tau} = 2.61 \times 10^5 P + 0.979 \frac{I}{N_b\sigma_z} \text{ [min}^{-1}], \quad (14)$$

where the units of P, I, and σ_z are Pa, mA, and mm, respectively. The coefficient of determination (R2) of the regression curve was 0.993. The dependence of τ calculated from Eq. (14) for currents with different N_b and pressure is presented in Figs. 13(b) and 14(b), respectively. The obtained regression curve is well correlated with the measured τ as shown in these figures.

The contribution of τ_p and τ_t to τ can be estimated by comparing the first and second terms on the right-hand side of Eq. (14). The ratio of the effect of τ_p and τ_t, or $(1/\tau_p)/(1/\tau_t)$, are plotted in Fig. 16 as a function of the bunch current (I/N_b) for different pressure ranges. In the range of I/N_b between 0.2 and 0.7 mA, the ratio was 0.4–0.2. At present, it was found that approximately 60%–80% of τ was determined by the Touschek lifetime (τ_t).

The lifetime determined by the Rutherford scattering, τ_r, is roughly estimated. τ_r is given by [37,41]

$$\frac{1}{\tau_r} = \frac{2\pi r_e^2 c}{k_B T \gamma^2} \frac{\beta_{ym}}{\alpha_{ym}^2} \sum_i \langle P_i(s)\beta_y(s)\rangle Z_i^2. \quad (15)$$

Here r_e is the classical electron radius (2.82×10^{-15} m), c is the speed of light (2.998×10^8 ms^{-1}), k_B is Boltzmann constant (1.381×10^{-23} J K^{-1}), T is the temperature [K], γ is the Lorentz factor, β_{ym} is the minimum vertical beta function and α_{ym} is the minimum vertical aperture, $P_i(s)$ is the partial pressure of the gas species i at the location s in the ring, $\beta_y(s)$ is the vertical beta function at the location s, and Z_i is the atomic number of the gas species i. Furthermore, the bracket represents an average along the

TABLE I. Sections and parameters used for the estimation of τ determined by the Rutherford scattering.

Sections	Length (m)	Ratio of section	Average β_y (m)	Average P (Pa)	Note
Interaction region (IR)	10	0.00332	265	1.90×10^{-6}	10 times of measured pressures just near IR
Local chromaticity correction section (Tsukuba)	316	0.105	82	6.25×10^{-8}	
Wiggler section (Nikko, Oho)	366	0.121	19	8.81×10^{-8}	
ARES cavity section (Fuji, Oho)	116	0.0385	18	3.10×10^{-7}	2 times of measured pressures in the storage cavities.
Arc section and others	2208	0.732	20	4.1×10^{-8}	
Average	(3016 in total)	(1.0 in total)	27	6.5×10^{-8}	

ring. As described above, the pressure is close to the measurement limit of the CCGs, so the value of each CCG reading could include large errors and is not reliable. Therefore, the average pressures at five representative sections in the ring were used where multiple CCGs values were included in each section. Table I shows the five sections, their lengths, ratios to the total length, average β_y, and average pressure in each section. The average pressure in the whole ring (except for those in the rf accelerating cavity section) was approximately 6×10^{-8} Pa in May 2022 ($I = 370$ mA, $N_b = 1662$). Assuming that the residual gas is completely CO (carbon monoxide), $\beta_{ym} = 12$ m and $\alpha_{ym} = 1$ mm (at the vertical collimator), $\langle P\beta_y \rangle = 3.23 \times 10^{-6}$ Pa m, the calculated τ_r was 72 min. The reciprocal of the first term on the right-hand side of Eq. (14) (τ_p) at $P = 6.5 \times 10^{-8}$ Pa is 59 min. The estimated τ_r is shorter than that calculated, but in agreement within a factor of 2.

For reference, the beam lifetimes determined by the Bremsstrahlung (τ_b) and Møller scattering (τ_m) were also estimated using the following equations [35,42]:

$$\frac{1}{\tau_b} = \frac{4\alpha r_e^2 c}{k_B T} \sum_i \langle P_i \rangle Z_i (Z_i + 1) \left(\frac{4}{3} \ln \frac{\gamma}{\gamma_c} - \frac{5}{6} \right)$$
$$\times \ln \left(183 Z_i^{-\frac{1}{3}} \right). \tag{16}$$

$$\frac{1}{\tau_m} = \frac{2\pi r_e^2 c}{k_B T} \frac{1}{\gamma_c} \sum_i \langle P_i \rangle Z_i. \tag{17}$$

Here α is the fine structure constant ($1/137$), $\gamma_c = \gamma \times \Delta E / E$, and $\Delta E / E$ is the rf-bucket height (0.5%). Assuming that the residual gas is CO and $P = 6.5 \times 10^{-8}$ Pa, the calculated values of τ_b and τ_m are approximately 85 and 3500 h, respectively, which are much longer than τ_r.

As for the HER, pressures are much lower than those of the LER, as shown in Figs. 4, 7, and 10. It is expected that τ is almost completely determined by the Touschek effect. Since the pressure is close to the measurement limit, a similar analysis using Eq. (13) is not reliable. Although the influence of pressure will be overestimated, we conducted a similar analysis to that of the LER using the data in Fig. 12(b) for the HER. Data points used are those when the values of current were larger than 100 mA, the values of τ were longer than 3 min, and the beam current was steadily decreasing for at least 1 min. No restriction was applied to the pressure, even when readings were close to the measurement limit (3×10^{-8} Pa) of the gauges. N_b were 783–2346 and I/N_b were in the range of 0.1–0.5 mA per bunch. The number of data points used was 1534.

The dependences of τ versus beam current for different N_b are shown in Fig. 17(a). τ depends on N_b as well as the total beam current and is longer with more bunches and the same beam current stored (smaller I/N_b), similar to the LER. The MRA was performed under the conditions that $1/\tau$ is zero when $P = 0$ Pa and $I = 0$ mA. The obtained regression curve for the HER was

$$\frac{1}{\tau} = 6.64 \times 10^4 P + 0.390 \frac{I}{N_b \sigma_z} \ [\text{min}^{-1}]. \tag{18}$$

Here the units of P and σ_z are Pa and mm, respectively. The coefficient of determination (R2) of the regression curve was 0.980. The dependence of τ calculated from Eq. (18) versus beam current for different N_b is shown in Fig. 17(b). The obtained regression curve is well correlated to the measured τ in these figures. Compared to the case shown in Fig. 16, the dependence of τ on pressure is very small.

The contribution of τ_p and τ_t to the τ can be estimated by comparing the first and second terms on the right-hand side of Eq. (18). The ratio of the effect of τ_p and τ_t, or $(1/\tau_p)/(1/\tau_t)$, are plotted in Fig. 18 as a function of I/N_b. In the range of the bunch current of 0.2–0.5 mA, the ratio was 0.2–0.1. It was found that approximately 80%–90% of the lifetime was determined by the Touschek lifetime (τ_t) for the HER case. The influence of pressure is even smaller than for the LER. Note that the influence of $1/\tau_p$ will be overestimated at low bunch currents where the measured pressure is near the measurement limit of the CCGs.
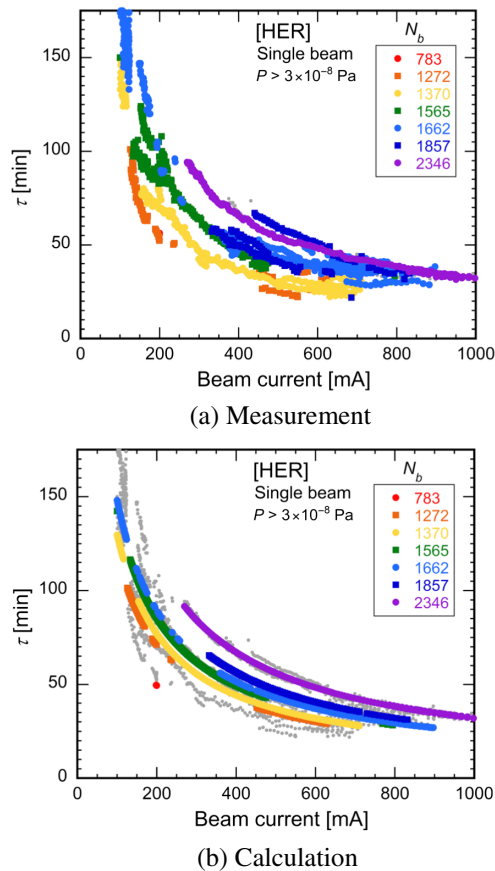
(a) Measurement

(b) Calculation

FIG. 17.　Dependence of τ on I (a) measured and (b) calculated using the regression curve for several N_b of 783–2346 from the 15th of March to the 22nd of June 2022 for the HER. Gray points correspond to all measured data.
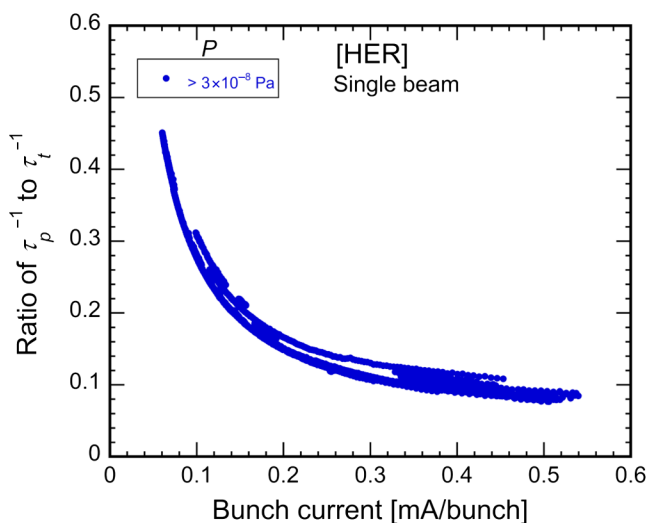

FIG. 18.　Ratio of the first term $(1/\tau_p)$ to the second term $(1/\tau_t)$ of the right-hand side of Eq. (18) for the HER.

V. ELECTRON CLOUD EFFECT IN LER

The electron cloud effect (ECE) is one of the most critical issues for high-intensity positron or proton storage rings, and the LER is no exception [43,44]. Here, the electron cloud effect (ECE) includes beam instabilities (oscillations), beam-size blowup, nonlinear pressure rises with increasing current, to name a few. All of these are caused by the formation of electron clouds (EC), which are high-density areas of electrons around the beam. Countermeasures adopted in the LER against the ECE are summarized in Table II, and the typical views of each countermeasure are shown in Fig. 19. Before starting Phase-1 commissioning, most of the counter-measures except for magnetic fields in the beam direction (B_z) had been installed.

Despite these various countermeasures, ECE was first observed during Phase-1 commissioning with a stored beam current of ~600 mA and a bunch filling pattern of 1/1576/3.06rf [4,5]. Here "1/1576/3.06rf" means a bunch filling pattern of one train with 1576 bunches and a bunch spacing of 3.06 rf buckets on average. One rf bucket is approximately 2 ns. The vertical beam size began to blow up once approximately 600 mA was being stored. At the same time, $\Delta P/\Delta I$ increased nonlinearly with increasing beam current due to multipacting of electrons [30,45]. The threshold of the linear current density (I_{d_th}) at which the beam size began to blow up was approximately 0.1–0.12 mA per bunch per rf bucket. This was observed with the different bunch filling patterns of 4/150/2rf, 4/150/3rf, 4/150/4rf, and 4/150/6rf and is shown in Fig. 20(a). Here, the linear current density (I_d) is the bunch current divided by the bunch spacing in the rf bucket. Although this I_{d_th} is much higher than that during the initial stages of the KEKB era (~0.04 mA bunch^{-1} rf bucket^{-1}) [46], it was smaller than expected. It was finally determined that this ECE was caused by EC in the Al-alloy bellows chambers without TiN-film coating on the inside.

To counteract the ECE, two units of permanent magnets (PMs) creating a magnetic field in the beam direction (B_z) of approximately 100 G were placed at the top and bottom of each Al-alloy bellows chamber (Fig. 21). This has considerably reduced the ECE.

The beam-size blowup began to appear again at $I \sim$ 900 mA with a bunch filling pattern of 1/1576/3.06rf. The value of I_{d_th} was approximately 0.2 mA per bunch per rf bucket, as shown in Fig. 20(b). It was observed that the electron density (n_e) around the beam was close to the anticipated threshold of electron density (n_{e_th}) where ECE would appear, that is, approximately 3×10^{11} m^{-3} [47], even in a region with TiN-film coating and antechambers. Transverse coupled bunch instabilities, with modes caused by electrons at drift spaces, were also detected [48]. The drift spaces refer to the spaces between electromagnets. From these observations, EC was considered to exist in the beam pipes in drift spaces, even though they have ante-chambers and TiN-film coating.

TABLE II. Countermeasures used to minimize the ECE in the SuperKEKB LER. The circular dots indicate the countermeasures applied for each main section in the ring.

Sections	Length (m)	n_e (circular) (m^{-3})	Antechamber (1/5)	TiN coating (3/5)	Solenoid (B_z;1/50)[a]	Groove (1/2)	Electrode (1/100)	n_e (expected m^{-3})
				Countermeasures				
Drift space (arc)	1629	8×10^{12}	•	•	•			2×10^{10}
Corrector magnets	316	8×10^{12}	•	•	•			2×10^{10}
Bending magnets	519	1×10^{12}	•	•		•		6×10^{10}
Wiggler magnets	154	4×10^{12}	•	•[b]			•	5×10^9
Quadrupole and Sextupole magnets	254	4×10^{10}	•	•				5×10^9
rf cavity section	124	1×10^{11}		•	•			1×10^9
IR	20	5×10^{11}		•	•			6×10^9
Total	3016							
Average		5.5×10^{12}						2.4×10^{10}

[a]Uniform magnetic fields in the beam direction are assumed.
[b]Except for beam pipes with clearing electrodes.
Abbreviations: rf cavity section: Beam pipes around rf cavities, IR: Interaction region.
n_e (circular): Density of electrons expected for circular beam pipe (copper).
n_e (expected): Density of electrons expected after applying countermeasures.
Antechamber: Antechamber scheme, Solenoid: Solenoid winding, but actually applying a magnetic field in the beam direction (B_z).
Groove: Beam pipe with grooves, Electrode: Beam pipe with clearing electrodes.

As additional countermeasures, PM units and solenoids were attached to most of the beam pipes in drift spaces after Phase-1 commissioning. The PM units with C-shaped Fe yokes (Type-1 PM units), and those consisting of Al-alloy cylinders with PMs inside (Type-2 PM units), were placed in series around the beam pipe as shown in Fig. 21 and
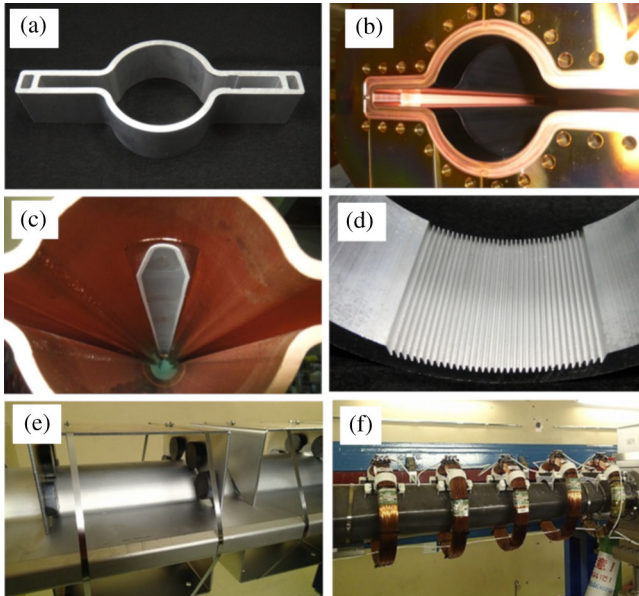

FIG. 19. Typical views of countermeasures adopted to the SuperKEKB LER: (a) beam pipes with antechambers, (b) TiN-film coating, (c) clearing electrode, (d) groove structure, magnetic fields in the beam direction by (e) permanent magnets and (f) solenoids.

produced $B_z \sim 60$ and 100 G, respectively. A simulation using the CLOUDLAND code [49] showed that n_e around the beam inside of the PM units is reduced to approximately $1/10$ of n_{e_th}, even with the designed beam parameters. Before starting Phase-2 commissioning, approximately 86% of the total drift space (approximately 2 km) was covered with B_z higher than 20 G, which value was found to be enough to reduce n_e below n_{e_th} based on simulations [13].

Figure 20(c) shows the dependence of the vertical beam size on I_d for different bunch filling patterns of 4/120/2rf, 4/120/3rf, and 4/120/4rf during Phase-2 commissioning. The beam size blowup was not observed until $I_d = 0.4$ mA per bunch per rf bucket [7]. Note that this I_d value is the maximum value that can be stored stably at this time in single-beam mode. I_{d_th} increased by at least twofold relative to that during Phase-1 commissioning [Fig. 20(b)]. The modes excited by electrons trapped by B_z near the inner wall were detected instead of those excited by the electrons around the beam [50]. The additional of B_z along the beam direction produced by the PM units and solenoids before Phase-22 commissioning began was found to effectively suppress the ECE.

Since ECE was observed at I_{d_th} lower than expected in Phase-1 commissioning, the effectiveness of the antechambers to suppress photoelectrons and the TiN-film coating to decrease the secondary electron yield (δ_{max}) in the beam pipes was reevaluated. This was done with different methods using simulations and experiments during Phase-2 commissioning [13]. Although the results were relatively scattered, it was found that the effectiveness of the antechamber with regard to the suppression of photoelectrons is smaller than
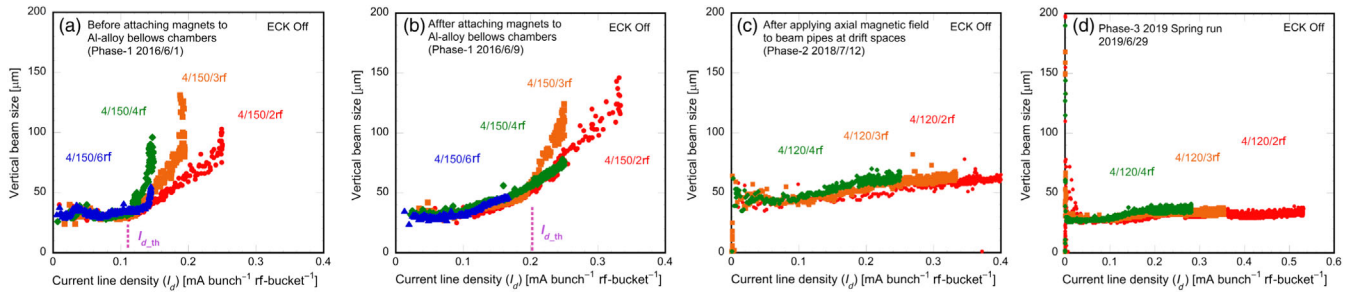
FIG. 20. Vertical beam sizes as a function of the current line density (I_d) for several bunch filling patterns measured (a) before and (b) after attaching PM units to Al-alloy bellows chambers in Phase-1 commissioning, (c) Phase-2 commissioning, and (d) Phase-3 commissioning.

that expected from the KEKB experiments [25]. This discrepancy can be explained as follows. More photons from SR generated by upstream bending magnets hit the beam channel due to the vertical opening angle and scattering in the real machine than in the experimental setup from KEKB. This indicates the importance of carefully estimating the effect of photoelectrons on ECE in the real machine [51,52]. For δ_{max} of the TiN-film coating, the estimated values were close to, or somewhat better than, those obtained in the laboratory [26]. The TiN-film coating seems to be working as expected with regard to reducing the emission of secondary electrons.

Before starting Phase-3 commissioning, additional PM units were added in the drift spaces, increasing the coverage from 86% to approximately 91% of the total drift space. In June 2019, vertical beam sizes and modes of instabilities were measured with a single stored beam. The change in the vertical beam sizes against I_d of 2–4 rf bucket spacing is shown in Fig. 20(d). No beam size blowup was observed until an I_d value of 0.53 mA per bunch per rf bucket, which was approximately 2.6 times higher than that during Phase-1 commissioning [Fig. 20(b)]. Note that this I_d value is the maximum value that can be stored stably in single-beam mode at that time. Coupled-bunch instabilities related to EC around the beam were not observed. The I_d value of
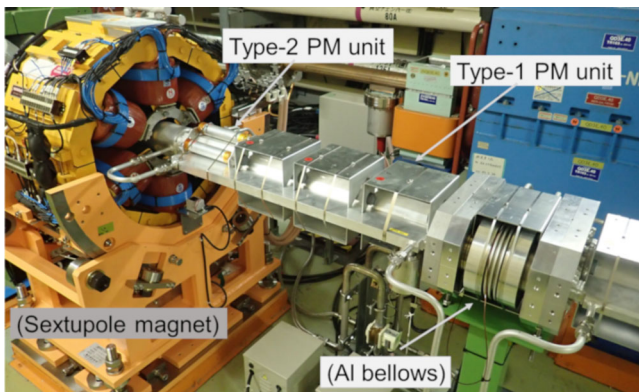
0.53 mA per bunch per rf bucket corresponds to approximately 2.6 A with a bunch filling pattern of 1/2400/2rf.

As supporting evidence of the absence of a beam-size blowup caused by ECE during a physics run (colliding beam mode), the luminosity of each bunch was measured by the Zero Degree Luminosity Monitor (ZDLM) [53]. This measurement was made with a bunch filling pattern of 2/1173/2.04rf and a beam current of 1250 mA in June 2022 (Fig. 22). This corresponds to the Id value of approximately 0.26 mA per bunch per rf bucket. Almost all parts of the trains have two rf bucket spacing. As seen in Fig. 22, the

FIG. 21. PM units attached to an Al-alloy bellows chamber, and Type-1 and Type-2 PM units for beam pipes at drift spaces.
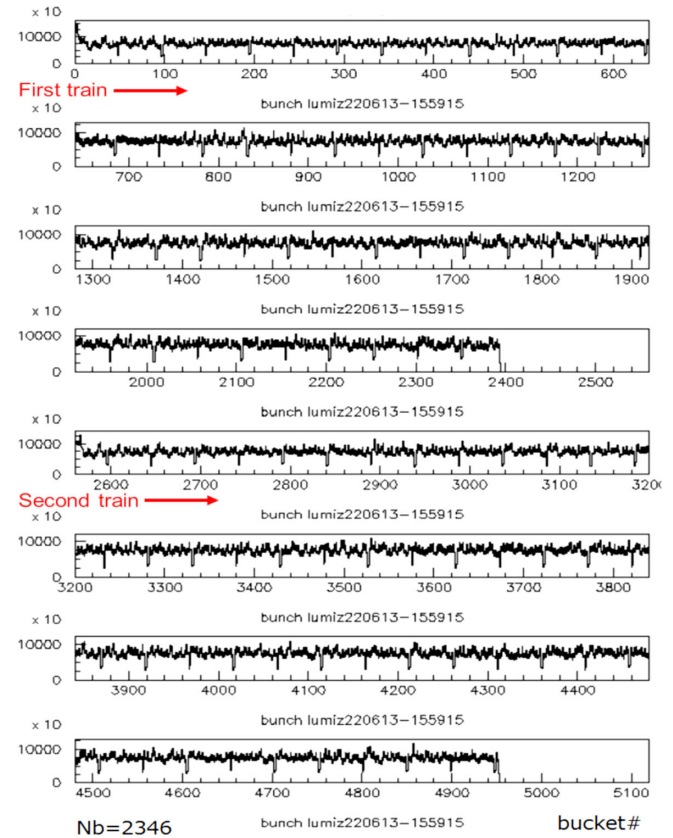

FIG. 22. Bunch-by-bunch luminosity for a bunch filling pattern of 2/1173/2.04rf on the 13th of June 2022. The vertical axis shows the number of hits at each ZDLM channel.

bunch luminosity is almost constant along the train, with no apparent "long-term" change in either train. One explanation of the high hit rate at the beginning of each train (i.e., bunch number 1–15 and 2561–2575) is due to the effects of the dead time and pile up of the detector circuit, nonuniformity of the bunch current, and beam-beam effect. Proving this explanation will require further analysis [54]. As indicated in Fig. 22, there is no degradation in the luminosity along the train, which would result from a beam-size blow-up caused by ECE.

In a recent single-beam mode operation, a vertical beam-size blowup was observed at a bunch current of approximately 0.8 mA per bunch, independent of the bunch filling pattern [3,55]. The frequency corresponding to $\nu_y - \nu_s$, where ν_y is the vertical betatron tune and ν_s is the synchrotron tune, was observed. This instability was called "−1 mode instability." The instability is not caused by ECE but is related to beam impedance, primarily due to the beam collimators. Further investigation to understand the mechanism of this instability is required.

VI. PRESSURE BURSTS ACCOMPANIED BY BEAM LOSS

One concern that has been recognized since Phase-1 commissioning is the localized pressure bursts (typically on the order of 10^{-7} Pa) accompanied by beam losses, which are typically observed in the LER. Beam loss monitors detect these losses and trigger a beam abort each time this occurs [4,5,56]. A typical pressure burst is shown in Fig. 23. Figures 24(a) and 24(b) show operational information until the 22nd of June 2022 for the LER and HER, respectively. The plots show the numbers of bursts occurring per 50 h of operation time (red bars) and the beam currents (I) at which the pressure bursts occurred (blue and green squares). The maximum current each day (I_{max}, pink dots), and locations of the pressure bursts along the ring as a function of the integrated operation time (duration time when $I > 50$ mA) are also shown. During Phase-1
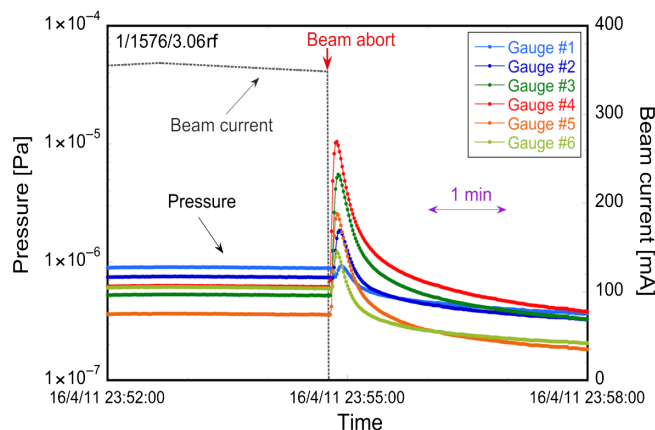

FIG. 23. Typical pressure bursts accompanied by beam loss (beam abort) observed in Phase-1 commissioning.

commissioning, most of the pressure bursts occurred near or inside new beam pipes installed during the upgrade period. In the LER, pressure bursts were frequently observed near or inside the Al-alloy beam pipes with grooved surfaces in dipole magnets. The beam current at which the bursts occurred increased gradually with I_{max}.

The most probable cause of these pressure bursts is the collision between the circulating beams and small dust particles in the beam pipes. Longitudinal grooves in the beam pipes of the LER for dipole magnets, which were added to counteract ECE, are likely to trap dust particles during the manufacturing process. These pressure bursts and simultaneous beam losses at $I \sim 800$ mA were artificially reproduced several times by "knocking" a beam pipe in a dipole magnet, which caused dust particles to drop from the upper area of the beam pipes [56]. Similar beam-loss phenomena have been observed at the Large Hadron Collider (LHC) at CERN and are referred to as the unidentified falling object problem [57,58].

During the shutdown period after Phase-1 commissioning, we gathered dust particles from two beam pipes in the LER around Tsukuba section in which pressure bursts had been frequently observed. Al and Al_2O_3 particles were found in one of the beam pipes. We "knocked" 24 beam pipes in the Tsukuba section in which pressure bursts were frequently observed, causing dust particles to drop from their upper surfaces prior to starting Phase-2 commissioning.

The frequency of pressure bursts was greatly reduced during Phase-2 commissioning, as shown in Fig. 24. However, the frequency decreased not only in the beam pipes around the Tsukuba section but also at other locations in the LER and HER. Therefore, it was not clear that the "knocking" of the beam pipes was effective. During Phase-2 commissioning, the operation time with high beam currents was much shorter than that during Phase 1, which may be one of the reasons for the pressure burst frequency reduction. An aging or conditioning effect is reported, which seems to have lowered the likelihood of a pressure burst at currents lower than the previously stored maximum beam current (I_{max}).

This phenomenon has been carefully monitored after starting Phase-3 commissioning. As shown in Fig. 24, the frequency of pressure bursts continues to occur at almost the same level for both the LER and HER, gradually increasing with I_{max}. In the early stage of Phase-3 commissioning (2019 and 2020), most beam pipes inside bending magnets in the LER were "knocked," as was performed in the Phase-1 commissioning in Tsukuba section. The effectiveness of the knocking has not been clearly observed to date.

From Phase-3 commissioning, the locations of the pressure bursts are limited to D02, D06, and D07 sections for the LER, and D08 and D09 sections for the HER, where "D##" refers to the name of the local control buildings along the ring (please refer to Fig. 26 below). These positions correspond to the location of the beam collimators. One reason is due to the
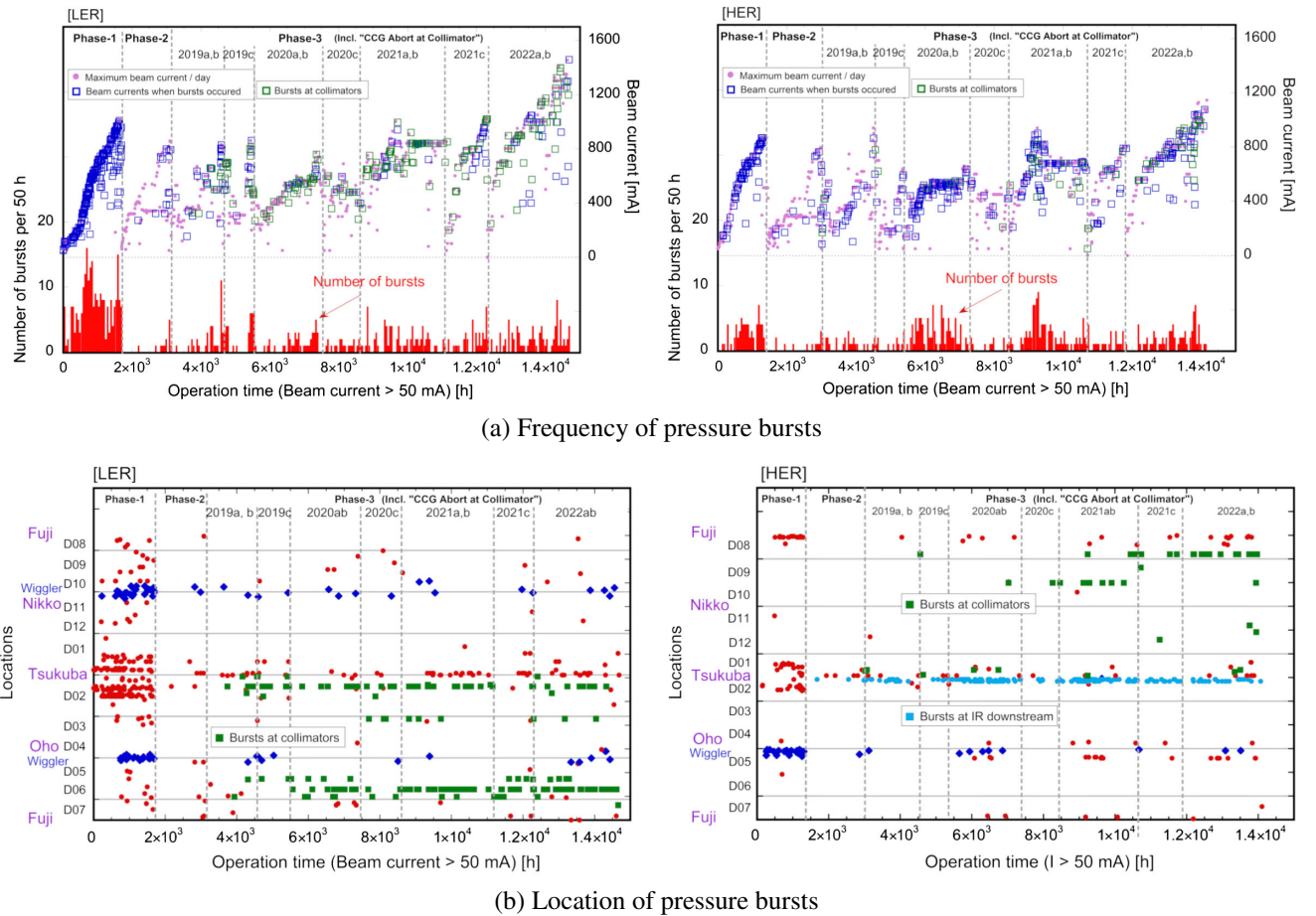
(a) Frequency of pressure bursts

(b) Location of pressure bursts

FIG. 24. (a) Number of bursts occurring per 50 h of operation time (red bars), the beam currents at which pressure bursts occurred (blue and green squares), I_{max} (pink dots), and (b) locations of the pressure bursts along the ring versus the operation time from 2016 for the LER (left) and HER (right). Green solid squares and light-blue solid squares in (b) are the locations at beam collimators and at just downstream of IR, respectively.

fact that the apertures of the beam collimators are small, typically 1–2 mm for vertical-type collimators in order to suppress the background of the Belle II detector [29,36]. The unstable beams could likely hit the collimator blades. Another reason is that a rapid beam abort system was introduced by watching small pressure rises ($\sim 1 \times 10^{-7}$ Pa) at the collimators. For the HER, in addition to the locations of the beam collimator, the pressure bursts are frequent just downstream of the interaction region (IR). The pressure bursts are thought to be caused by SR emitted from strong magnets near the IR due to unstable beams. This seems likely because the pressure was sensitive to the beam orbit and the size of the beam at the IR. The main cause of pressure bursts after Phase-2 and Phase-3 commissioning is due to the impact of abnormal beams or SR on beam collimators or beam pipes rather than the collision of the beams with dust particles in the beam pipe.

At present, one critical challenge in the operation is the heavy beam loss that occurs within two or three turns (20–30 μs). The beam suddenly becomes unstable and can directly hit the vertical-type collimator heads. This has also led to quenches of the superconducting magnets at IR [3,59]. This event is referred to as the "sudden beam loss" and is more frequent for the LER. The cause of the sudden beam loss has not been identified yet. One possible cause is the collision of the beam with dust in the beam pipe, which could result in the energy loss of the beam. Pressure bursts are sometimes observed at beam pipe locations other than the beam collimators at the same time. However, up to now, simulations cannot explain the sudden loss due to collisions of the beam with dust particles. In the simulations, most of the beams should be lost at the horizontal-type collimators rather than the vertical-type collimators [59]. The severe damage to vacuum components such as the rf-shield bellows chamber can be another cause of beam loss [60]. No indication of deterioration, such as the increase in temperature or pressure in these areas has been observed. Further investigation into this sudden beam loss will be pursued in the future.

VII. OTHER MAJOR CHALLENGES

A. Damages due to sudden beam losses and high impedances of beam collimators

The beam collimator is a special vacuum component used to reduce the background noise of the Belle II detector by removing the halo of the storage beam and removing particles with a large oscillation amplitude just after the injection to the MR [16,29]. New collimators were designed and installed for the LER and the Tsukuba section of the HER. The original collimators from KEKB were reused [61,62] for the arc sections of the HER. The structure of a vertical-type collimator and installation pictures for LER and HER are shown in Figs. 25(a) and 25(b), respectively. The collimator head is located within a few mm of the beam orbit and the position is controlled remotely with an accuracy of approximately 0.1 mm. The position was adjusted carefully while observing the beam orbit, background levels, and beam injection efficiency. The heads of the LER collimator were initially made of tungsten with a length of 10 mm but were gradually replaced by tantalum, as described later. The heads of the HER collimators for arc sections were made of titanium with a length of 40 mm. The locations of the collimators in the LER and HER are summarized in Fig. 26. The beam collimators have been successful at suppressing the background noise of the Belle II detector and preventing the superconducting magnets at the IR from quenching. Quenching of the superconducting magnets can be caused by the penetration of particles that have deviated from their ideal orbits [36].

One significant challenge for the beam collimator is the damage to the head as a result of a "sudden beam loss" event as described above. If enough energy is deposited on
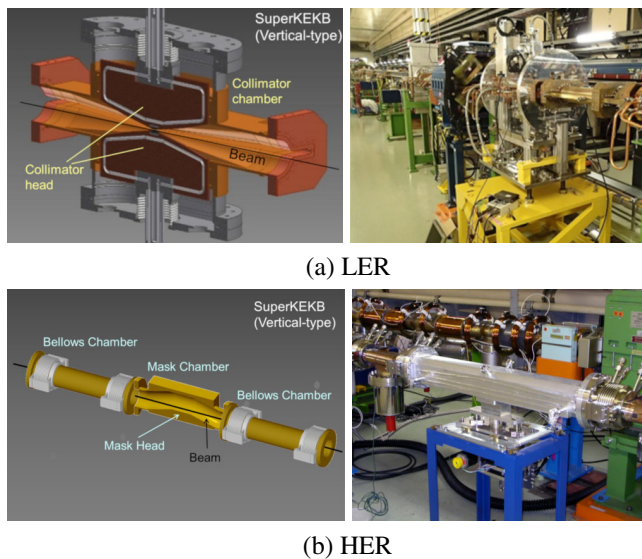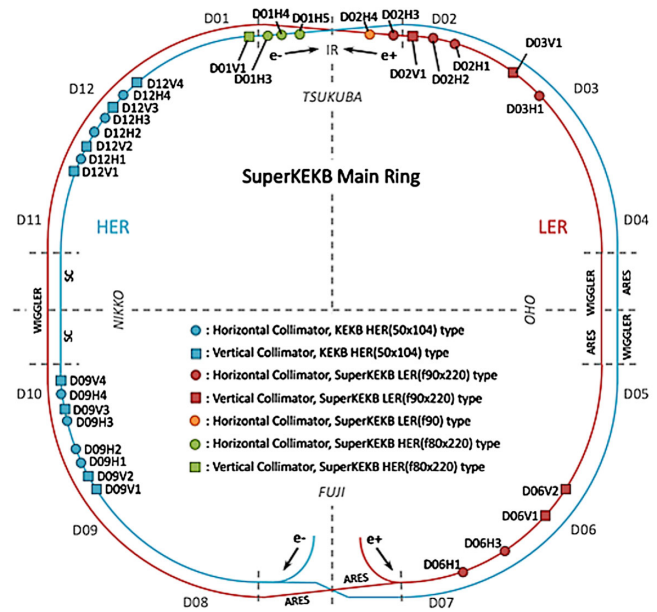

FIG. 26.   Location of collimators in the MR, where "H" and "V" in the collimator names refer to the horizontal and vertical collimators, respectively.

the head of the collimator, significant damage such as deep grooves and metal projections can result as shown in Fig. 27. The width of the groove was approximately 1 mm, which widened gradually in the beam direction (along the beam path). When a collimator head with this type of damage is brought close to the beam, the background noise in the Belle-II detector increases. As a temporary measure to mitigate this problem, the entire collimator chamber was moved approximately 2–3 mm in the horizontal direction to provide an undamaged surface in-line with the beam. This type of damage also indicates the brittleness of tungsten when high energy particles impact the surface. To reduce this risk, the head material of the LER collimators has been gradually exchanged for tantalum. The length of the collimator heads in the arc sections, where the tip scattering is less critical, was also

(a) LER

(b) HER

FIG. 25.   Schematic of beam collimator structures and those installed in the tunnel for (a) LER and (b) HER.
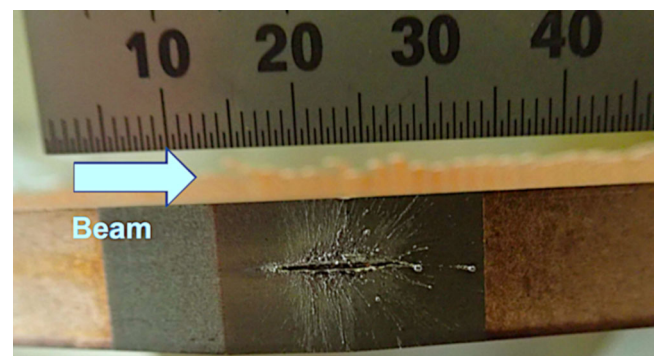

FIG. 27.   Typical damaged head in a vertical collimator, where the traveling direction of the beam is from left to right.

shortened to reduce the risk of damage. The damaged heads were eventually replaced during the subsequent shutdown period. As an alternative solution to this problem, a new collimator head made of carbon (graphite) has been developed [63]. Carbon has a high melting point compared to metals but, the radiation length is longer and the electric resistivity is higher, which leads to a higher impedance. Bonding to the base metal is also difficult. The R&D efforts, such as the copper coating on the beam-facing surfaces and brazing to copper using many narrow grooves, are currently ongoing.

Another challenge of the collimator is its high impedance to the beam. The collimator head is designed to have low geometric impedance by tapering the side walls (as shown in Fig. 25) and rf shielding to avoid trapped HOM [16]. Since the collimator head position is close to the beam orbit, it has a higher beam impedance than other components and contributes a major part of the total impedance budget of the ring. The high impedance leads to large tune shifts and excites beam instabilities, such as transverse mode coupling instability (TMCI) [55]. The threshold of the TMCI instability is very sensitive to the position of the collimator head as well as the operating point of tunes. During the long shutdown period in 2022 and 2023, a new collimator system, called a "nonlinear collimator," will be installed in the LER [3,64,65]. In this system, the aperture of the vertical collimator can be larger than in other locations by using a nonlinear kick in a local skew-sextupole magnet. With a larger gap, an impedance reduction is expected.

B. Heating of beam pipes and flanges in wiggler sections

The heating of several beam pipes and connection flanges in the LER wiggler sections [Fig. 28(a)] has been observed since Phase-1 commissioning [4,5]. A typical temperature is approximately $50\,^{\circ}\mathrm{C}$ with a stored beam current of approximately 1 A. It was found that the temperature of these components is sensitive to the vertical beam orbit upstream of these locations as shown in Fig. 29. The vertical positions of the beam pipes themselves are also critical. From these observations, it was concluded that the heating was due to the SR emitted from the wiggler magnets located upstream from the beam pipes in question. The beam pipes and connection flanges in the wiggler sections have a 14-mm high antechamber, (same as arc sections) through which most of the SR can pass. However, the antechamber cannot completely accommodate all of the SR emitted from the long wiggler sections when including small vertical misalignments of components and the vertical opening angle of the SR. This results in the upper and lower surfaces of the antechambers being irradiated. Since SR masks are typically located at the sides of the antechambers, they cannot fully shadow the connection flanges from the SR. Air leaks due to the excess heating were observed at vacuum flange joints while storing high beam currents in the 2022ab run (Fig. 30).
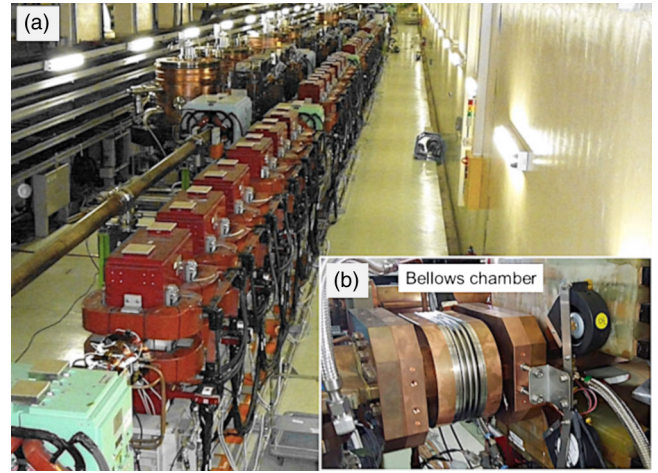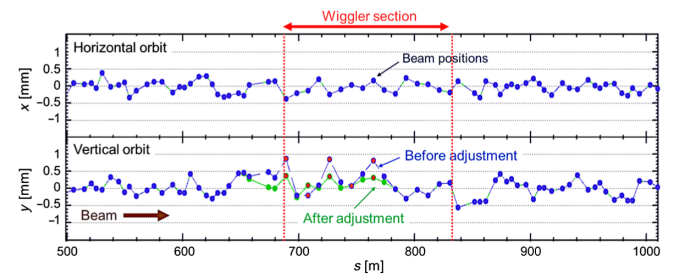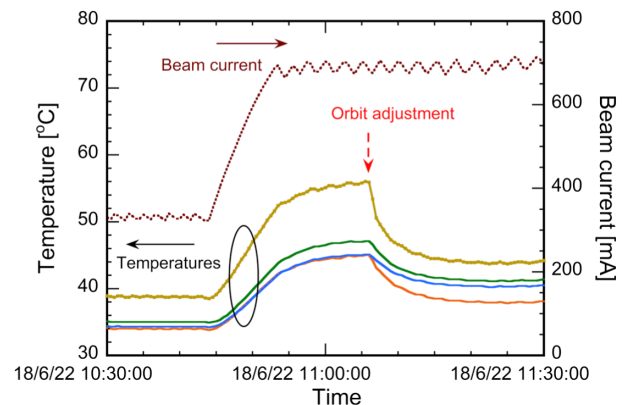

FIG. 28.   (a) Wiggler section in the LER (Oho) and (b) bellows chamber with cooling blowers.

To mitigate these issues, several countermeasures have been implemented. First, the beam pipes in these areas were realigned in the vertical direction. Second, the vertical beam orbit in the wiggler sections was adjusted to reduce

(a) Vertical orbit adjustment at wiggler section.

(b) Temperatures of beam pipes and beam current

FIG. 29.   (a) Adjustment of the vertical orbit at a wiggler section, where blue dots are the horizontal and vertical positions of the beam measured by beam position monitors placed almost every 10 m. The vertical orbit was adjusted from the dashed blue line to the green line by correction magnets. (b) Change in temperatures of several beam pipes in the wiggler section at the timing of the vertical orbit adjustment shown in (a).
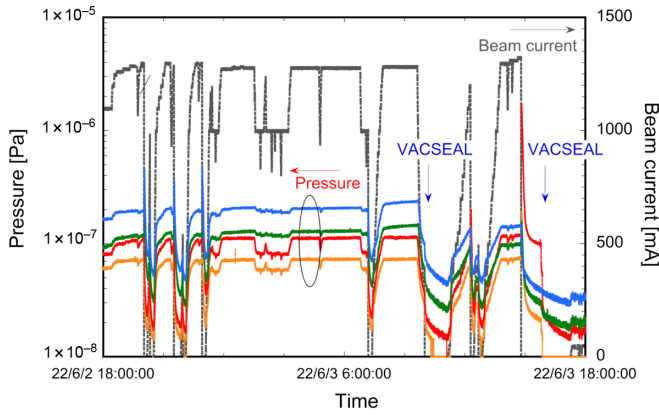
FIG. 30.   Behaviors of pressures and beam currents when air leak occurred at flanges in a wiggler section. The pressure increased at the time of beam aborts. The leaks were finally repaired by a liquid sealant (i.e., VACSEAL).

FIG. 32.   Trends of beam current and pressures around a beam pipe at the downstream of Oho wiggler section from 2022.

C. Water leak from cooling channels

the heating as much as possible. Third, the cooling water flow rate through the overheated beam pipes was increased. Finally, air blowers were installed around the beam pipes and flanges which displayed excessive heating to provide additional cooling [Fig. 28(b)].

In addition to the countermeasures mentioned above, new bellows chambers with SR masks at the top and bottom of the antechambers were designed and fabricated. These redesigned components will protect the flanges and gaskets from vertical misalignment and the widening SR fan. The inside of the bellows chamber is shown in Fig. 31. The new bellows chamber has functioned as expected and the temperatures of the flanges on the downstream side have decreased while the temperature of the bellow chamber increased as expected. Additional upgraded bellows chambers will be installed in these sections to relax the SR power on the masks. The cooling water flow rate will also be increased during the 2022 long shutdown period to remove the additional heat in these new bellows chambers.
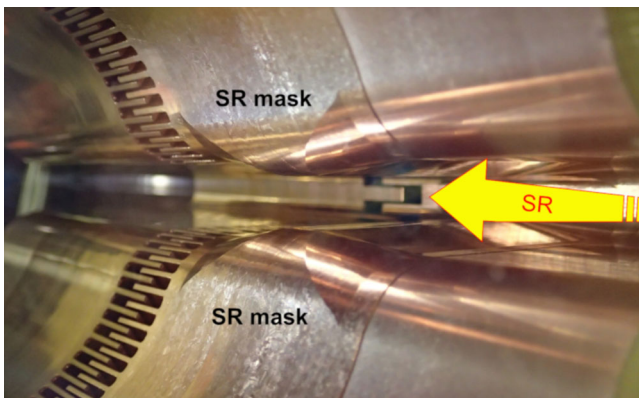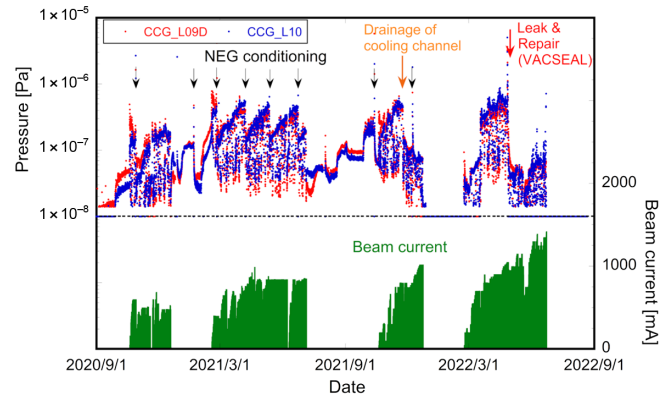
Unusual pressure behavior has been observed downstream of the OHO wiggler section during the past couple of years, as shown in Fig. 32. The pressure increased gradually over several months even without the beam in the ring but decreased after every NEG conditioning cycle. Although helium leak checks have been performed several times, no air leak was observed from the outside of the suspicious beam pipe [Fig. 33(a)]. In November 2021, the pressure decreased suddenly when the cooling channel of the beam pipe was drained but, the elevated pressure returned after several months. In April 2022, the pressure increased abruptly to an unprecedented level, as shown in Fig. 32. A careful He leak check was performed from the outside of the beam pipe and from the inside of the cooling channel. The pressure decreased rapidly when the cooling channel was drained. Finally, a leak was detected between the cooling channel and the beam channel after drying the cooling channels and pressurizing them with approximately 60 kPa of helium. It was not possible to locate the exact

FIG. 31.   Inside of a bellows chamber with SR masks at antechambers developed for wiggler sections.
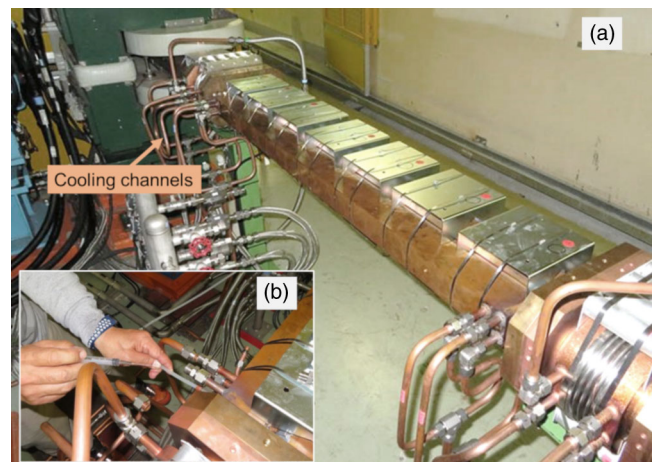

FIG. 33.   (a) Beam pipe at the downstream of Oho wiggler section and (b) spray of liquid sealant into the cooling channel.

location of the leak inside the cooling channel. A liquid sealant (VACSEAL, PASCAL Co. Ltd.) was sprayed from the inlets into the cooling channel while blowing dry nitrogen [Fig. 33(b)]. The leak was successfully sealed, and the pressure in the vacuum chamber decreased as shown in Fig. 32. To date, no increase in pressure has been observed but this area will be carefully monitored in the future.

D. Curious behaviors of pressure

While increasing the beam currents, curious behavior of the pressure has been observed at various times around the ring. One example is shown in Fig. 34, where the pressure of a vacuum gauge began to increase rapidly with constant beam current. The measured temperature of a nearby gate valve was also increasing during the same time. In this area, the beam pipe near the gate valve and vacuum gauge has a taper structure. Therefore, it was suspected that an excited HOM resonance due to the taper section began to heat the gate valve which led to higher thermal desorption and a rapid increase in pressure. It has been planned to move this gate valve far from the taper section during the long shutdown in 2022. Similar pressure behavior was also observed at another vacuum gauge and gate valve location in the ring.

Another example of unexpected pressure behavior is near one of the vertical-type beam collimators of the HER. This collimator is one of the preexisting KEKB-type collimators. The pressure rise became significant while storing higher beam currents. Since the pressure is very sensitive to the position of the collimator head, a HOM excited by the collimator can be a source of the heating or discharging resulting in an abnormal pressure rise. This condition does not differ from other vertical-type collimators and the actual cause has not been clearly understood yet. The inside of this particular collimator will be checked during the long shutdown in 2022.
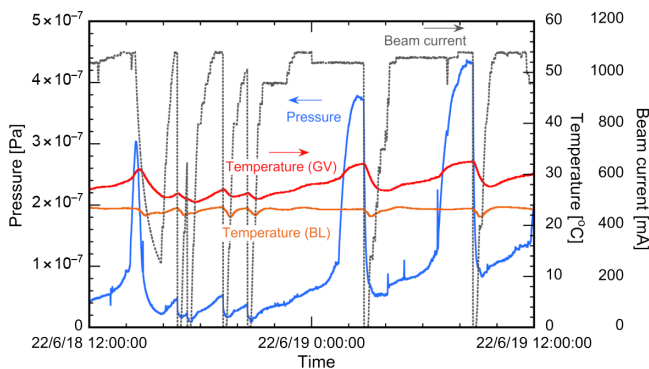

FIG. 34. Behaviors of the beam current, pressure, and temperatures of a gate valve (GV) and a bellows chamber (BL) on the 18th and 19th of June, 2022.

VIII. CONCLUSION

SuperKEKB is the first high-current accelerator to adopt several novel vacuum components on a large scale. Since the start of the Phase-1 commissioning in 2016, the vacuum system and newly adopted components have performed as expected. The pressure of both rings has decreased steadily, although the pressure in the LER is still higher than that of the HER. The recent high-current operation has started revealing the effect of thermal gas desorption due to the heating by wall currents and HOMs. The beam lifetimes are primarily determined by the Touschek effect for both rings in single-beam mode. The electron cloud effect (ECE) observed during Phase-1 commissioning was caused by EC in the Al-alloy bellows chambers which do not have TiN-film coating and in the beam pipes through drift spaces with TiN-film coating and antechambers. Countermeasures, such as the installation of PM units and solenoids after the Phase-1 commissioning have been working well, and no indication of ECE has been observed so far during operating conditions. After Phase 1, the frequency of pressure bursts has generally decreased, although they continue to be observed primarily at beam collimator locations. Damage to beam collimators caused by the sudden beam losses constitutes a serious challenge to the operation of the SuperKEKB. Research and development efforts are currently underway to develop robust collimator blades which can withstand these beam losses events. A new nonlinear collimator system is being prepared for installation with the expectation of reducing the impedance due to collimators. Countermeasures against the heating problems of the beam pipes at wiggler sections are also in progress. Curious pressure behaviors, which are suspected to be caused by HOMs, are becoming more noticeable as the beam currents increase. More careful monitoring of the vacuum system will be required in the future as the beam currents are increased toward the full design values.

The experiences of the vacuum system in the SuperKEKB provide valuable information to scientists and engineers in the accelerator vacuum field and provide insight for designing vacuum systems for future cutting-edge high-intensity accelerators.

ACKNOWLEDGMENTS

[1] SuperKEKB, https://www-superkekb.kek.jp/.

[2] Ohnishi *et al.*, Accelerator design at SuperKEKB, Prog. Theor. Exp. Phys. **2013**, 03A011 (2013).

[3] Y. Funakoshi *et al.*, The SuperKEKB has broken the world record of the luminosity, in *Proceedings of IPAC'22,*

Bangkok, Thailand (JACoW, Geneva, Switzerland, 2022), pp. 1–5, 10.18429/JACoW-IPAC2022-MOPLXGD1.

[4] Y. Suetsugu *et al.*, First commissioning of the SupeKEKB vacuum system, Phys. Rev. Accel. Beams **19**, 121001 (2016).

[5] Y. Suetsugu, K. Shibata, T. Ishibashi, K. Kanazawa, M. Shirai, S. Terui, and H. Hisamatsu, Achievements and problems in the first commissioning of SuperKEKB vacuum system, J. Vac. Sci. Technol. A **35**, 03E103 (2017).

[6] K. Shibata, Y. Suetsugu, T. Ishibashi, M. Shirai, , S. Terui, K.-I. Kanazawa, and H. Hisamatsu , Commissioning of vacuum system for SuperKEKB positron damping ring, J. Vac. Sci. Technol. A **37**, 041601 (2019).

[7] Y. Suetsugu, K. Shibata, T. Ishibashi, M. Shirai, S. Terui, K.-i. Kanazawa, and H. Hisamatsu, SuperKEKB main ring vacuum system status until the end of Phase-2 commissioning, J. Vac. Sci. Technol. A **37**, 021602 (2019).

[8] Y. Suetsugu, K.-i. Kanazawa, K. Shibata, T. Ishibashi, H. Hisamatsu, M. Shirai, and S. Terui, Design and construction of the SuperKEKB vacuum system, J. Vac. Sci. Technol. A **30**, 031602 (2012).

[9] Y. Suetsugu, K. Kanazawa, K. Shibata, T. Ishibashi, H. Hisamatsu, M. Shirai, and S. Terui, Construction status of the SuperKEKB vacuum system, Vacuum **121**, 238 (2015).

[10] Y. Suetsugu, K.-i. Kanazawa, K. Shibata, T. Ishibashi, H. Hisamatsu, M. Shirai, and S. Terui , Results and problems in the construction phase of the SuperKEKB vacuum system, J. Vac. Sci. Technol. A **34**, 021605 (2016).

[11] Y. Suetsugu, K. Shibata, T. Ishibashi, K. Kanazawa, M. Shirai, S. Terui, and H. Hisamatsu, Beam scrubbing of beam pipes during the first commissioning of SuperKEKB, Appl. Surf. Sci. **432, Part B**, 347 (2018).

[12] Y. Suetsugu, H. Fukuma, K. Ohmi, K. Shibata, and M. Tobiyama, Study to mitigate electron cloud effect in SuperKEKB, in *Proceedings of eeFACT2018, Hongkong, China* (JACoW, Geneva, Switzerland, 2018), pp. 95–102, 10.18429/JACoW-eeFACT2018-TUYAA04.

[13] Y. Suetsugu *et al.*, Mitigating the electron cloud effect in the SuperKEKB positron ring, Phys. Rev. Accel. Beams **22**, 023201 (2019).

[14] H. Koiso, Commissioning status of high luminosity collider rings for SuperKEKB, in *Proceedings of 8th International Particle Accelerator Conference, IPAC'17, Copenhagen, Denmark* (JACoW, Geneva, Switzerland, 2017), pp. 1275–1280, 10.18429/JACoW-IPAC2017-TUZB2.

[15] Belle II, https://www.belle2.org.

[16] T. Ishibashi, Y. Suetsugu, and S. Terui, Low impedance movable collimators for SuperKEKB, in *Proceedings of 8th International Particle Accelerator Conference, IPAC'17, Copenhagen, Denmark* (JACoW, Geneva, Switzerland, 2017), pp. 2929–2932, 10.18429/JACoW-IPAC2017-WEPIK009.

[17] Y. Suetsugu, H. Hisamatsu, T. Ishibashi, K. Kanazawa, K. Shibata, M. Shirai, and S. Terui, Problems in SuperKEKB vacuum system during the Phase-1 commissioning and their mitigation measures, in *Proceedings of 8th International Particle Accelerator Conference, IPAC'17, Copenhagen, Denmark* (JACoW, Geneva, Switzerland, 2017), pp. 2925–2982, 10.18429/JACoW-IPAC2017-WE-PIK008.

[18] Y. Ohnishi, Report on SuperKEKB Phase-2 commissioning, in *Proceedings of 9th International Particle Accelerator Conference, IPAC'18, Vancouver, BC, Canada* (JACoW, Geneva, Switzerland, 2018), pp. 1–5, 10.18429/JACoW-IPAC2018-MOXGB1.

[19] Y. Suetsugu, H. Hisamatsu, T. Ishibashi, K. Kanazawa, K. Shibata, M. Shirai, and S. Terui, Status of the SuperKEKB vacuum system in the Phase-2 commissioning, in *Proceedings of 9th International Particle Accelerator Conference, IPAC'18, Vancouver, BC, Canada* (JACoW, Geneva, Switzerland, 2018), pp. 2833–2835, 10.18429/JACoW-IPAC2018-WEPML059.

[20] A. Morita, Status of early SuperKEKB Phase-3 commissioning, in *Proceedings of 10th International Particle Accelerator Conference, IPAC'19, Melbourne, Australia* (JACoW, Geneva, Switzerland 2019), pp. 2255–2257, 10.18429/JACoW-IPAC2019-WEYYPLM1.

[21] Y. SuetsuguK. Shibata, and M. Shirai, Design study of distributed pumping system using multilayer NEG strips for particle accelerators, Nucl. Instrum. Methods Phys. Res., Sect. A **597**, 153 (2008).

[22] K. Shibata, Y. Suetsugu, T. Ishibashi, M. Shirai, S. Terui, K.-i. Kanazawa, H. Hisamatsu , Vacuum system of positron damping ring for SuperKEKB, J. Vac. Sci. Technol. A **35**, 03E106 (2017).

[23] Y. Suetsugu, K. Kanazawa, K. Shibata, M. Shirai, A. E. Bondar, V. S. Kuzminykh, A. I. Gorbovsky, K. Sonderegger, M. Morii, and K. Kawada, Development of bellows and gate valves with a comb-type rf-shield for high-current accelerators, Rev. Sci. Instrum. **78**, 043302 (2007).

[24] Y. Suetsugu, M. Shirai, M. Ohtsuka, T. Nishidono, K. Watanabe, Y. Suzuki, M. Tsuchiya, A. Yonemoto, K. Sennyu, and H. Hara , Development of copper-alloy Matsumoto–Ohtsuka-type vacuum flanges and its application to accelerator beam pipes, J. Vac. Sci. Technol. A **27**, 1303 (2009).

[25] Y. Suetsugu *et al.*, R&D of copperbeam duct with antechamber scheme for high current accelerators, Nucl. Instrum. Methods Phys. Res., Sect. A **538**, 206 (2005).

[26] K. Shibata, H. Hisamatsu, K. Kanazawa, Y. Suetsugu, and M. Shirai, Development of TiN coating system for beam ducts of KEK B-factory, in *Proceedings of the 11th European Particle Accelerator Conference, Genoa, 2008* (EPS-AG, Genoa, Italy, 2008), pp. 1700–1702, https://accelconf.web.cern.ch/e08/papers/tupp071.pdf.

[27] Y. Suetsugu, H. Fukuma, K. Shibata, M. Pivi, and L. Wang, Beam tests of a clearing electrode for electron cloud mitigation at KEKB Positron Ring, in *Proceedings of the International Particle Accelerator Conference, Kyoto, Japan* (ICR, Kyoto, 2010), pp. 2369–2371, https://accelconf.web.cern.ch/IPAC10/papers/weoamh01.pdf.

[28] Y. Suetsugu, H. Fukuma, M. Pivi, and L. Wang, Continuing study on electron-cloud clearing techniques in high-intensity positron ring: Mitigation by using groove surface in vertical magnetic field, Nucl. Instrum. Methods Phys. Res., Sect. A **604**, 449 (2009).

[29] T. Ishibashi, S. Terui, Y. Suetsugu, K. Watanabe, and M. Shirai, Movable collimator system for SuperKEKB, Phys. Rev. Accel. Beams **23**, 053501 (2020).

[30] Gröbner, A. G. Mathewson, , H. Störi, P. Strubin, and R. Souchet , Studies of photon induced gas desorption using synchrotron radiation, Vacuum **33**, 397 (1983).

[31] C. L. Foerster, C. Lanni, and K. Kanazawa , Measurements of photon stimulated desorption from thick and thin oxide of KEKB collider copper beam chambers and a stainless-steel beam chamber, J. Vac. Sci. Technol. A **19**, 1652 (2001).

[32] J. M. Lafferty, *Foundations of Vacuum Science and Technology* (John Wiley & Sons, Inc., New York, 1997), ISBN: 978-0-471-17593-3.

[33] P. A. Thiel and T. E. Madey, The interaction of water with solid surfaces: Fundamental aspects, Surf. Sci. Rep. **7**, 211 (1987).

[34] A. W. Chao, K. H. Mess, M. Tigner, and F. Zimmermann, *Handbook of Accelerator Physics and Engineering* (World Scientific Publishing Co. Pte Ltd., Singapore, 1998), ISBN: 978-981-4415-84-2.

[35] J. Le Duff, Current, and current density limitations in existing electron storage rings, Nucl. Instrum. Methods Phys. Res., Sect. A **239**, 83 (1985).

[36] A. Natochii, S. E. Vahsen, H. Nakay, T. Ishibashi, and S. Terui, *et al.*, Improved simulation of beam backgrounds and collimation at SuperKEKB, Phys. Rev. Accel. Beams **24**, 081001 (2021).

[37] W. Heitler, *The Quantum Theory of Radiation*, 3rd ed. (Oxford University Press, London 1954), ISBN: 978-0486645582.

[38] B. Nash, F. Ewald, L. Farvacque, J. Jacob, E. Plouviez, J. L. Revol, and K. Scheidt, Touschek lifetime and momentum acceptance measurements for ESRF, in *Proceedings of the 2nd International Particle Accelerator Conference, San Sebastián, Spain* (EPS-AG, Spain,2011), pp. 2921–2923, https://accelconf.web.cern.ch/IPAC2011/papers/thpc008.pdf.

[39] E. Mulyani, J. W. Flanagan, H. Fukuma, H. Ikeda, and M. Tobiyama, Image reconstruction techniques based on coded aperture imaging for SuperKEKB X-Ray beam Size Monitor, in *Proceedings of 9th International Particle Accelerator, IPAC'18, Vancouver, BC, Canada* (JACoW,Geneva, Switzerland, 2018), pp. 4819–4822, 10.18429/JACoW-IPAC2018-THPML074.

[40] G. Mitsuka, Beam monitors (XRM, SRM, Loss mon., FB), in *Proceedings of the 23rd KEKB Accelerator Review* (KEK, 2019). https://www-kekb.kek.jp/MAC/2019/Report/Mitsuka.pdf.

[41] E. Fischer, Residual gas scattering, beam intensity and interaction rate in proton storage rings, CERN Report No. ISR-VAC/67-16, 1967, http://cds.cern.ch/record/296970/files/196700231.pdf.

[42] N. F. Mott, *The Theory of Atomic Collisions*, 2nd ed. (Oxford University Press, London 1949). ISBN: 978-0198520306.

[43] K. Ohmi and F. Zimmermann, Head-Tail Instability Caused by Electron Clouds in Positron Storage Rings, Phys. Rev. Lett. **85**, 3821 (2000).

[44] F. Zimmermann, Review of single-bunch instabilities driven by an electron cloud, Phys. Rev. ST Accel. Beams **7**, 124801 (2004).

[45] Y. Suetsugu, Observation and simulation of the nonlinear dependence of vacuum pressures on the positron beam current at the KEKB, in *Proceedings of the Particle Accelerator Conference, Chicago, IL, 2001* (IEEE, New York, 2001), pp. 2183–2185. https://accelconf.web.cern.ch/p01/PAPERS/WPAH043.PDF.

[46] H. Fukuma *et al.*, Observation of vertical beam blow-up in KEKB low energy ring, in *Proceedings of the European Particle Accelerator Conference, Vienna, 2000* (EPS, Geneva, 2000), pp. 1122–1124, https://accelconf.web.cern.ch/e00/PAPERS/WEP5A12.pdf.

[47] Y. Susaki and K. Ohmi, Electron cloud instability in SuperKEKB low energy ring, in *Proceedings of the International Particle Accelerator Conference, Kyoto, Japan* (ICR, Kyoto, 2010), pp. 1545–1547, https://accelconf.web.cern.ch/IPAC10/papers/tupeb014.pdf.

[48] K. Ohmi, J. Flanagan, H. Fukuma, H. Ikeda, E. Mulyani, K. Shibata, Y. Suetsugu, and M. Tobiyama, Electron cloud studies in SuperKEKB phase I commissioning, in *Proceedings of the international Particle Accelerator Conference, IPAC'17, Copenhagen, Denmark* (JACoW, Geneva, Switzerland, 2017), pp. 3104–3106, 10.18429/JACoW-IPAC2017-WEPIK074.

[49] L. F. Wang, H. Fukuma, K. Ohmi, S. Kurokawa, K. Oide, and F. Zimmermann, Numerical study of the photoelectrons cloud in KEKB low energy ring with a three-dimensional particle in cell method, Phys. Rev. ST Accel. Beams **5**, 124402 (2002).

[50] S. S. Win, K. Ohmi, H. Fukuma, M. Tobiyama, J. Flanagan, and S. Kurokawa, Numerical study of coupled-bunch instability caused by an electron cloud, Phys. Rev. ST Accel. Beams **8**, 094401 (2005).

[51] J. A. Crittenden, D. Sagan, T. Ishibashi, and Y. Suetsugu, Synchrotron radiation analysis of the SuperKEKB positron ring, in *Proceedings of 6th International Particle Accelerator Conference, IPAC'15, Richmond, VA* (JACoW, Geneva, Switzerland, 2015), pp. 2222–2224, 10.18429/JACoW-IPAC2015-TUPTY080.

[52] G. G. Cantón, F. Zimmermann, G. H. I. M. Cuna, and E. D. Ocampo, Electron cloud buildup for LHC 'Sawtooth' vacuum chamber, in *Proceedings of 9th International Particle Accelerator Conference, IPAC'18, Vancouver, BC, Canada* (JACoW, Geneva, Switzerland, 2018), pp. 744–746, 10.18429/JACoW-IPAC2018-TUPAF030.

[53] T. Hirai, S. Uehara, and Y. Watanabe, Real-time luminosity monitor for a B-factory experiment, Nucl. Instrum. Methods Phys. Res., Sect. A **458**, 670 (2001).

[54] S. Uehara, private communication (2022).

[55] S. Terui, H. Fukuma, Y. Funakoshi, T. Ishibashi, T. Nakamura, K. Ohmi, Y. Ohnishi, M. Tobiyama, and R. Ueki, The report of machine studies related to the vertical beam size blow-up in SuperKEKB LER, in *Proceedings of 13th International Particle Accelerator Conference, IPAC'22, Bangkok, Thailand* (JACoW, Geneva, Switzerland, 2022), pp. 2169–2172, 10.18429/JACoW-IPAC2022-WEPOTK050.

[56] S. Terui, H. Hisamatsu, T. Ishibashi, K. Kanazawa, K. Shibata, M. Shirai, and Y. Suetsugu, Observation of pressure bursts in the SuperKEKB positron ring, in *Proceedings of 9th International Particle Accelerator Conference, IPAC'18, Vancouver, BC, Canada*(JACoW,

Geneva, Switzerland, 2018), pp. 2830–2832, 10.18429/JACoW-IPAC2018-WEPML058.

[57] A. Lechner *et al.*, Beam loss measurements for recurring fast loss events during 2017 LHC operation possibly caused by macroparticles, in *Proceedings of 9th International Particle Accelerator Conference, IPAC'18, Vancouver, BC, Canada* (JACoW, Geneva, Switzerland, 2018), pp. 780–783, 10.18429/JACoW-IPAC2018-TUPAF040.

[58] L. K. Grob, M. Dziadosz, E. B. Holzer, A. Lechner, B. Lindstrom, R. Schmidtpresenter, D. Wollmann, and C. Zamantzas, Analysis of loss signatures of unidentified falling objects in the LHC, in *Proceedings of 9th International Particle Accelerator Conference, IPAC'18, Vancouver, BC, Canada* (JACoW, Geneva, Switzerland, 2018), pp. 814–817, 10.18429/JACoW-IPAC2018-TU-PAF049.

[59] S. Terui, Y. Funakoshi, H. Hisamatsu, T. Ishibashi, K. Kanazawa, Y. Ohnishi, K. Shibata, M. Shirai, Y. Suetsugu, and M. Tobiyama, Report on collimator damaged event in SuperKEKB, in *Proceedings of 12th International Particle Accelerator Conference, IPAC'21, Campinas, SP, Brazil* (JACoW, Geneva, Switzerland, 2021), pp. 3541–3544, 10.18429/JACoW-IPAC2021-WEPAB359.

[60] M. K. Sullivan *et al.*, Anomalous high radiation beam aborts in the Pep-II B-Factory, in *Proceedings of the 10th European Particle Accelerator Conference, Edinburgh, Scotland, 2006* (Edinburgh, Scotland, 2006), pp. 652–654, https://accelconf.web.cern.ch/e06/PAPERS/MOPLS049.PDF.

[61] Y. SuetsuguK. Shibata, T. Sanami, T. Kageyama, and Y. Takeuchi, Development of movable mask system to cope with high beam current, Rev. Sci. Instrum. **74,** 3297 (2003).

[62] Y. Suetsugu, T. Kageyama, K. Shibata, and T. Sanami, Latest movable mask system for KEKB, Nucl. Instrum. Methods Phys. Res., Sect. A **513,** 465 (2003).

[63] S. Terui, T. Abe, Y. Funakoshi, T. Ishibashi, H. N. Nakayama, K. Ohmi, D. Zhou, and A. Natochii, Development of low-Z collimator for SuperKEKB, in *Proceedings of 12th International Particle Accelerator Conference, IPAC'21, Campinas, SP, Brazil* (JACoW, Geneva, Switzerland, 2021), pp. 3537–3540, 10.18429/JACoW-IPAC2021-WEPAB358.

[64] N. Merminga, J. Irwin, R. Helm, and R. D. Ruth, Collimation systems for a TeV Linear Collider, Report No. SLAC-PUB-5165-Rev., 1994, https://www.slac.stanford.edu/pubs/slacpubs/5000/slac-pub-5165.pdf.

[65] A. Faus-Golfe and F. Zimmermann, A nonlinear collimation system for CLIC, Report No. CERN-SL-2002-032 (AP), CLIC Note 520, 2002, https://cds.cern.ch/record/561146/files/sl-2002-032.pdf.